https://doi.org/10.5194/wes-2026-94
Preprint. Discussion started: 11 June 2026

eawe european academy of wind energy
Open Access WIND ENERGY SCIENCE DISCUSSIONS

How accurate is the beam position of scanning lidars? An intercomparison

Matthew Young[1], Matthew Docherty[1], Lin-Ya Hung[2], Andy Oldroyd[1], and Julia Gottschall[2,3]

[1]Oldbaum Services Limited, Stirling, UK
[2]Fraunhofer Institute for Wind Energy Systems IWES, Bremerhaven, Germany
[3]Faculty of Geosciences, University of Bremen, Germany

Correspondence: Matthew Young (m.young@oldbaum.co.uk) and Julia Gottschall (julia.gottschall@iwes.fraunhofer.de)

Abstract. Scanning wind lidar provide a flexible measurement solution to accurately quantify near-shore and offshore wind resource and site conditions to help reduce risk and costs for prospective offshore wind developments. Typically these devices are set up using a near-horizontal beam position (elevation angle) in order to obtain wind speed measurements at distances of 3-10 km at heights in the atmospheric boundary layer relevant to wind turbines. Consequently, precise knowledge of the beam position and any associated positioning errors of the lidar scan head is required to minimise the uncertainty in the measurement height and thus the resulting wind speed measurements. A number of Hard Target Testing (HTT) methods are typically used to determine and correct for beam position errors, and include the use of static hard targets (SHT; e.g. buildings), dynamic hard targets (DHT; i.e. drone) and the sea surface itself (Sea Surface Levelling; SSL). However, to-date, these methods have not been consistently compared. This paper therefore systematically compares the performance of the SHT, DHT and SSL methods in determining the static elevation angle error (elevation offset) for scanning lidar wind measurement campaigns. A comparison experiment is conducted using two independent pulsed scanning lidar devices (type Vaisala WindCube 400S) at a near-shore wind measurement test site in the UK, using an offshore meteorological mast as the static reference hard target across all methodologies. Differences in the mean elevation offset relative to the reference target range from $-0.03°$ to $-0.20°$ for SHT, $-0.002°$ for DHT, and from $-0.05°$ to $+0.07°$ for SSL. The uncertainties found from the methods range from approximately $\pm 0.03°$ for DHT to up to $\pm 0.20°$ for SSL. Overall, the results show that in the absence of offshore static hard targets, the DHT method can reliably determine the elevation offset with lowest uncertainty. While practically easier to execute, the SSL method showed more varying results between the two devices tested and exhibited larger uncertainties due to a number of factors including the determination of the sea surface distance, sea state and device tilt. When performed thoroughly, the elevation offset can be obtained from all methods to within the specified angular positioning error ($\pm 0.1°$) of the scanning lidar model. While the SSL method exhibits larger uncertainties, it offers an alternative approach when resources (e.g. suitable SHT candidates) are limited and can be implemented regularly to quantify time-dependent angular drifts for both near-shore and offshore applications.

https://doi.org/10.5194/wes-2026-94
Preprint. Discussion started: 11 June 2026

eawe european academy of wind energy
Open Access WIND ENERGY SCIENCE DISCUSSIONS

1 Introduction

Offshore wind energy is a key contributor to the renewable energy mix required for a rapid energy transition away from fossil fuels (The Crown Estate, 2025; Wind Europe, 2026; Global Wind Energy Council, 2026). Accurately quantifying offshore wind and site conditions is therefore critical to reducing the risks and thus costs for future offshore wind farm developments. Wind measurements from floating wind lidar technology are widely deployed by the offshore wind industry to obtain high-quality measurements of the wind resource in replacement of traditional meteorological masts (Gottschall et al., 2017). However, in recent years, scanning lidars have been increasingly utilised due to their ability to measure at long-range and setup flexibility to retrieve wind field measurements across a diverse range of use-cases including measurements of wind speed and turbulence (Peña and Mann, 2019; Shimada et al., 2022, 2025), quantification of horizontal wind field gradients and wind farm wakes (Trujillo et al., 2011; Wang and Barthelmie, 2015; Krishnamurthy et al., 2017; Bodini et al., 2017; Schneemann et al., 2020; Cañadillas et al., 2022; Hildebrand et al., 2025), and model evaluation (Menke et al., 2020; Goit et al., 2020; Hung et al., 2022). Whilst scanning lidar are capable of providing cup-anemometer equivalent wind speed measurements (Shimada et al., 2022, 2025), their commercial adoption relies on understanding and quantifying all sources of measurement uncertainties to mitigate potential risks for future large-scale offshore wind projects.

Measurement campaigns using one or more scanning lidar devices deployed onshore at the coastline provide a cost-effective way of obtaining high-quality wind resource measurements at distances of 3-10km offshore from the coast (Shimada et al., 2025). In order to accurately measure winds at such distances, precise knowledge of the beam position and any associated positioning errors is required. In the lidar reference frame, the beam position is expressed by its horizontal direction via the azimuth angle θ and vertical direction relative to the horizontal plane via the elevation angle ϕ. To measure winds at distances of 3–10 km at heights relevant to wind turbines of approximately 50–300 m, ϕ is small (i.e. $< 5\ ^\circ$). Thus the corresponding height of the beam is highly sensitive to small ϕ variations ($\triangle\phi$) driven by device inclination and the internal alignment of the scan head (Gramitzky et al., 2026). Due to vertical wind shear within the atmospheric boundary layer, the resulting height variations can lead to large deviations in the measured wind speed and thus the predicted power generation (Gramitzky et al., 2026). As such, minimising $\triangle\phi$ is critical for maximising wind speed measurement accuracy, particularly as wind lidar technology advances towards longer range measurements where the same $\triangle\phi$ leads to larger height variations than near-range measurements. Compared to offshore measurement campaigns where devices have to be placed on dynamic platforms such as the wind turbine transition piece or nacelle, devices deployed onshore for near-shore campaigns are usually placed on a static, non-moving surface. This means that for near-shore campaigns, temporal variations in device inclination and their contribution to $\triangle\phi$ are expected to be small, therefore allowing static ϕ errors primarily due to the internal alignment of the scan head to be quantified.

When deploying scanning lidar devices, beam positioning is calibrated via Hard-Target Testing (HTT) which is used to determine the precise beam location relative to truth (Vasiljević et al., 2016; Champneys et al., 2024). The Static Hard Target (SHT) method consists of aiming the laser beam at a static hard object with a clear edge profile (e.g. corner of building or mast) and known position, determined using suitable site surveying methods, such as via a total station. The position at which the

https://doi.org/10.5194/wes-2026-94
Preprint. Discussion started: 11 June 2026

eawe european academy of wind energy
Open Access WIND ENERGY SCIENCE DISCUSSIONS

beam hits the object in the reference frame of the lidar is determined from the peak in the lidar return signal (e.g. the carrier-to-noise-ratio; CNR). This position in the lidar reference frame is compared with the expected true position of the object relative to the location of the device from which any possible pointing errors are identified and then corrected for by applying angular offset(s) to measurement setup.

While performing beam position calibration via HTT is easier onshore due to a greater likelihood of viable SHT candidates (in structure, direction and range) near the deployment location, calibration for near-shore and offshore deployments is more challenging due to a lack of available targets in the desired offshore measurement direction where the beams are pointed towards the location of a future offshore wind farm development as part of the pre-construction wind resource and site condition assessments. In a near-shore scenario, theoretically the simplest approach is to perform a single-SHT test, provided that the SHT is located directly in the desired pointing direction of the measurements. However, the existence of a suitable SHT in an undeveloped offshore location is highly unlikely. Alternatively, a multi-SHT calibration process can be performed where the SHT procedure is executed using at least 3 individual hard targets positioned at different θ which are then used to fit a sinusoidal function to determine the angular offsets as a function of θ (Champneys et al., 2024; Oldroyd et al., 2024). While this method is less restrictive than the single SHT approach, its viability depends on the existence of suitable static targets with sufficient azimuthal spacing to ensure the quality of the sinusoid fit in capturing the underlying angular offsets, which is not always possible depending on the situation of the deployment. In such cases, a single SHT can be used in combination with device rotation, where the lidar body is physically rotated $\theta = 90°$ and the single SHT is repeated each time to build up the sinusoid (NEDO, 2023). However, this approach is time consuming and assumes consistent device leveling per rotation.

To overcome these limitations, recent studies have focused on extending the HTT approach by using drones (Thorsen et al., 2023; Oldroyd et al., 2024) and the sea surface itself (Rott et al., 2022; Gramitzky et al., 2024, 2026). Dynamic Hard Targeting (DHT) using drones is advantageous as the drone can be remotely flown to a specific location relative to the lidar device, equivalent to the desired measurement angles, from which it can be acquired by the laser beam to determine the relative beam position to truth and any resulting angular offsets. The drone approach has been shown to be successful both for drone acquisition, where the lidar is used to scan a hovering drone, and beam acquisition, where the drone is flown into a fixed laser beam (Oldroyd et al., 2024). Alternatively, Sea Surface Levelling (SSL) methods involve scanning the sea surface and using the drop in the lidar return signal (e.g. CNR) to identify the range at which the laser beam is absorbed by the water surface (Rott et al., 2022; Gramitzky et al., 2024, 2026). Sea surface scans were initially employed to estimate device tilt on the transition piece of offshore wind turbines, hence defined as "Sea Surface Levelling" (Rott et al., 2022; Gramitzky et al., 2024, SSL). However, the SSL method has been further extended to estimate the lidar elevation angle offset and lidar height in addition to device tilt, showing promising results (Gramitzky et al., 2026).

While SSL methods show promising results in the context of offshore scanning lidar measurement campaigns installed on the dynamic transition piece of a wind turbine, there is currently no evidence evaluating their performance in a coastal environment where there are a number of challenges. First, devices deployed onshore may have a narrow field of view of the sea surface depending on the local surroundings, limiting their ability to scan across a large enough area to obtain sufficient measurements for calibration. Second, coastal seas experience larger tidal ranges than offshore, and also variable wave conditions including

https://doi.org/10.5194/wes-2026-94
Preprint. Discussion started: 11 June 2026

eawe european academy of wind energy
Open Access WIND ENERGY SCIENCE DISCUSSIONS

breaking waves, which are likely to increase the uncertainty of the SSL methods (e.g. Gramitzky et al., 2026). Despite this, coastal deployments experience much smaller device tilt compared to offshore devices installed on a moving transition piece. Therefore the absence of significant device tilt is expected to partially reduce the uncertainty of SSL methods when applied in a coastal situation. However, during movement of the scanner head, even if a device is perfectly level its inclination may vary due the weight of the scan head, and hence may add additional uncertainties even for a static deployment.

In this paper, we compare the performance of the three primary HTT methodologies available for determining the elevation angle offsets for scanning lidar wind measurement campaigns. The study builds upon methods applied in an initial SHT and DHT (drone) intercomparison experiment implemented as part of an operational wind measurement campaign (Oldroyd et al., 2024). The comparison experiment is conducted using two independent pulsed doppler scanning lidar devices at a near-shore wind measurement test site in the UK. We compare SHT, DHT (drone) and SSL methods using an offshore meteorological mast as a static reference hard target for all methodologies. We also estimate the pointing uncertainties determined from the different methodologies, to build up an understanding of their performance and suitability for scanning lidar wind measurement campaigns. In doing this we seek to answer the following questions: 1) Do different HTT methodologies provide consistent estimates of the elevation angle offsets?, 2) Which methodology has the smallest uncertainty? and, 3) Which method performs best?

Section 2 of this paper describes the experiment setup and HTT methodologies. Section 3 presents results from the different methods applied in the context of a measurement campaign. This is followed by a discussion of the results in Section 4 and the resulting conclusions in Section 5.

2 Methodology

2.1 Lidar coordinate system and beam alignment

The translation between lidar and reference coordinate systems forms the basis of the HTT methods evaluated in this study. The beam coordinate system consists of an azimuth angle (θ) expressing the beam direction in the horizontal plane and elevation angle (ϕ) expressing the inclination of the beam relative to the horizontal plane (Fig. 1). The range r, is the distance along the beam from the scan head at which a measurement is obtained. Figure 1 illustrates the applicability of this coordinate system for two common scanning strategies; a Plan Position Indicator (PPI) scan, where ϕ is constant and θ varies, and Range Height Indicator (RHI) scan, where θ is constant and ϕ varies. Misalignment between lidar (θ_{lidar}, ϕ_{lidar}) and truth (θ_{ref}, ϕ_{ref}), stem from the lidar orientation and leveling, and alignment of the laser optics and scan head mechanism. As such, offsets

$$\theta_{\text{off}} = \theta_{\text{lidar}} - \theta_{\text{ref}} \tag{1}$$

$$\phi_{\text{off}} = \phi_{\text{lidar}} - \phi_{\text{ref}} \tag{2}$$

https://doi.org/10.5194/wes-2026-94
Preprint. Discussion started: 11 June 2026

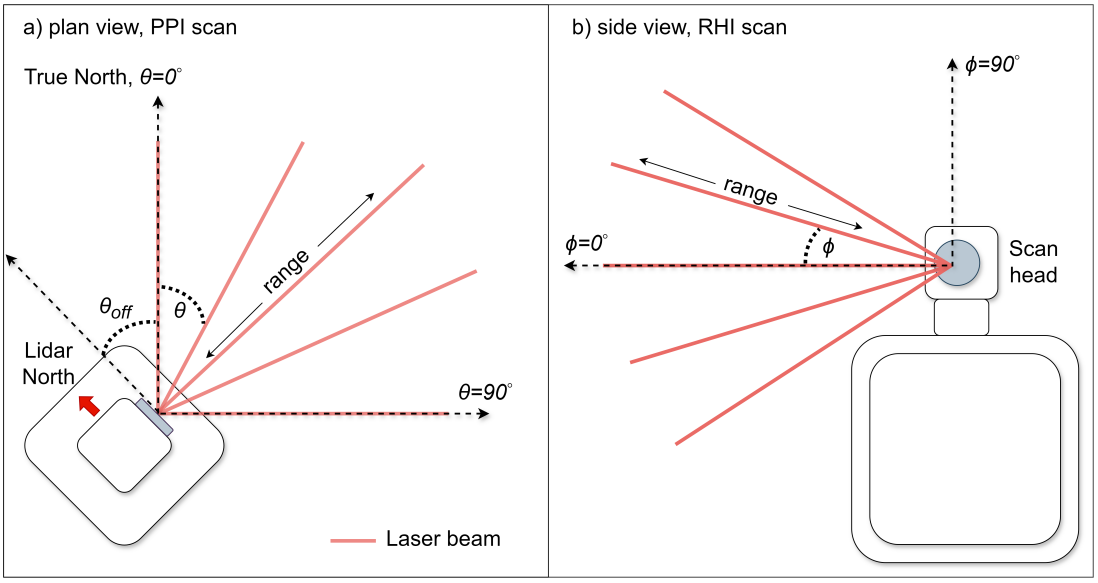

Figure 1. Illustration of the scanning lidar coordinate system from a) plan view for a Plan-Position Indicator (PPI) scan and b) side view for a Range Height Indicator (RHI) scan.

are applied to the desired measurement setup to account for misalignment of the lidar beam from truth. θ_{off} and ϕ_{off} are determined via HTT methods, which are based on the principle of recording θ_{lidar} and ϕ_{lidar} at the beam intersection point with an object with θ_{ref} and ϕ_{ref} where the intersection point is identified from the backscatter signal of the laser beam. Typically this approach performs multiple PPI scans at consecutive elevation angles, resulting in a CNR map of the target. Determining θ_{ref} and ϕ_{ref} requires the precise coordinates (x,y,z) of both the lidar scan head and object to be known which are typically acquired using a total station survey. Both θ_{off} and ϕ_{off} are assumed to vary sinusoidally with θ_{lidar} due to the scan head mechanism (e.g. Oldroyd et al., 2024; Champneys et al., 2024) and can be expressed via

$$\phi_{\text{off}} = A\sin(\theta_{\text{lidar}} + P) + O \tag{3}$$

where A is the amplitude, P is the phase and O is the offset of the sinusoid. This function allows ϕ_{off} at the desired θ of the measurement campaign to be determined from the resulting curve fit. In this study we focus on quantifying ϕ_{off} as opposed to θ_{off} since vertical variations in horizontal wind speed are expected to be larger than horizontal variations and thus the vertical positioning of the beam has a larger impact on the measurement uncertainty.

2.2 Experiment Setup

We focus on comparing three HTT methodologies – Static Hard Target (SHT), Dynamic Hard Target (DHT) using drone, and Sea Surface Levelling (SSL) - used to determine ϕ_{off} which are relevant for, but not limited to, nearshore deployments. Figure

https://doi.org/10.5194/wes-2026-94
Preprint. Discussion started: 11 June 2026

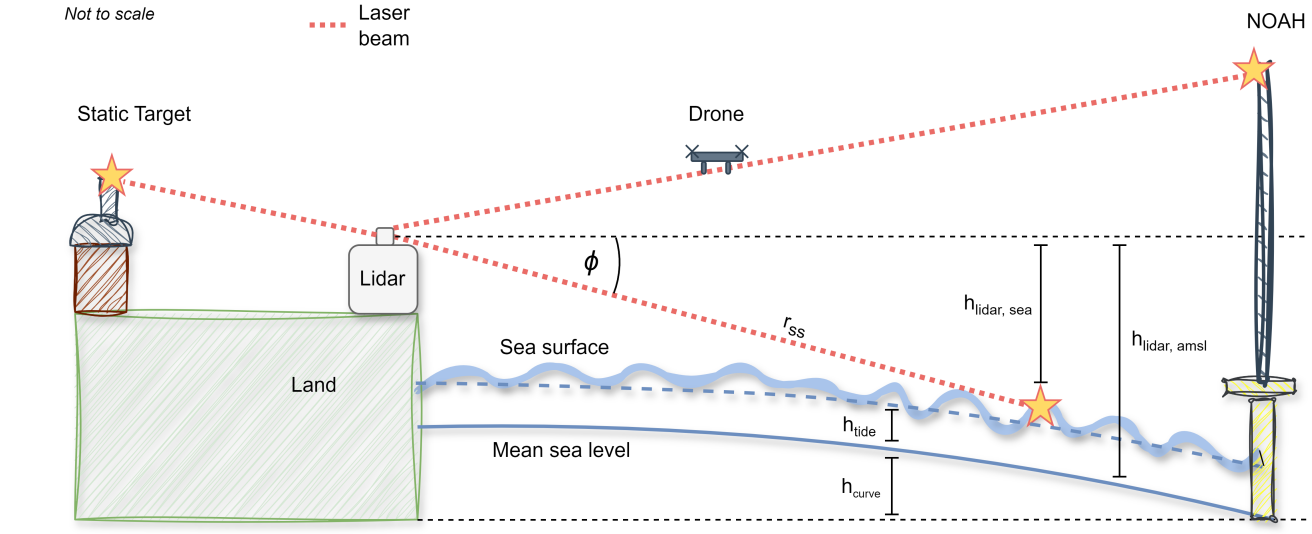

Figure 2. Diagram illustrating the coastal hard target experiment showing side view of scanning lidar device and example beam geometry with respect to reference hard target (NOAH met mast), static hard target, drone and sea surface. Diagram not to scale.

2 and Figure 3 provide an overview of the various components and geometry of the experiment. The experiment was carried out over a 9-day period 22nd April 2025 – 30th April 2025 using two Vaisala WindCube Scan 400S scanning lidar devices of generations v2.1 and v2.0 (SL South and SL North, Table 1) deployed as part of a near-shore measurement campaign at the Centre for the Testing of Environmental Sciences Technology (C-TEST) test site near Blyth, UK, based around the Offshore Renewable Energy Catapult's (OREC) National Offshore Anemometry Hub (NOAH) 103 m above mean sea level (amsl) tall offshore meteorological mast (Fig. 3). SL South and SL North are deployed onshore at a distance from NOAH of approximately 5330 m and 6840 m, respectively. Note that the two scanning lidars have different scanner head driver mechanisms; SL South is belt driven, whereas SL North is gear driven. The specified angular pointing accuracy of both devices by the manufacturer is $\pm 0.1°$.

The geometry of the test was specifically designed to facilitate comparison among the three HTT methods. The height of the top cup anemometer at 103 m on the NOAH mast is treated as the primary reference static hard target to determine ϕ_{off} exactly at the desired pointing direction and location for a wind measurement campaign. Cup anemometers at 35 m and 69 m were also used as additional reference targets for redundancy. Onshore SHT candidates are used to test the suitability of applying a multi-SHT approach to derive ϕ_{off} using targets opposite to the desired measurement direction (Fig. 3). For the DHT method, multiple drone flights were performed from SL South to three locations at 500 m distance offshore corresponding to the equivalent pointing azimuth of SL South to NOAH, and $\theta_{\text{ref}} \pm 35°$ azimuth either side of NOAH (Fig. 3). Drone flights were limited to a distance of 500 m due to flight restrictions. For the SSL method, PPI and RHI scans were performed by both

https://doi.org/10.5194/wes-2026-94
Preprint. Discussion started: 11 June 2026

eawe european academy of wind energy
Open Access WIND ENERGY SCIENCE DISCUSSIONS

Table 1. Overview of Vaisala WindCube scanning lidar device details used during experiment. The specified angular pointing accuracy of the devices is $\pm 0.1^{\circ}$

Name	Serial Number	Scan Head Driver	Generation
SL South	WCS001072	Belt	v2.1
SL North	WCS000319	Gear	v2.0

SL South and SL North over a 24-hour period on 29th April 2025. For comparison, these scans were aligned with the relative directions of NOAH and the drone flights.

A site survey using a total station was used to determine the precise position (x,y,z) of the lidar scanner heads, static hard targets, and drone flights. As the test spanned multiple days, the total station was set up in a global coordinate system (WGS84). We setup the total station using the resection from three known positions (Ghilani and Wolf, 2012). The total station setup uncertainty is hence estimated from the resection's residuals, which were on the order of $\sim$0.02 m. Accounting for target geometry and angular errors that occurred during the survey, the expected accuracy of the site survey coordinates is within 0.1 m.

Due to the coastal location of the experiment and thus a greater expected impact of tidal levels on the SSL results than further offshore, tidal gauge measurements at North Shields, located 14.1 km south of SL South, were obtained from the UK National Tide Gauge Network (https://environment.data.gov.uk/flood-monitoring/tidegauge/index.html). The tidal measurements provide the tide level relative to mean sea level (ordnance datum) at a temporal frequency of 15 min. During the SSL test period (28 to 30 April 2025), the tidal levels ranged from a minimum of -2.25 m below mean sea level to a maximum of $+2.95$ m above mean sea level thus with a full tidal range of 5.20 m. Wave conditions during the test were also obtained from a Datawell Directional WaveRider Mk III buoy (Newbiggin Waverider) measuring as part of the Northeast Regional Coastal Monitoring Programme (https://coastalmonitoring.org/). The Newbiggin Waverider buoy is located 1.6 km east of SL North and 6.3 km north from SL South. During the test period wave conditions were calm with significant wave heights < 0.5 m and maximum heights < 0.7 m measured by the wave buoy.

2.3 Hard Target Testing Methods

This section provides details on the setup and implementation of the three HTT methods employed in the experiment. Each method is used to determine ϕ_{off} as a function of azimuth, from which Eq. (3) is applied to estimate ϕ_{off} across all azimuths. Table 2 shows the different device settings applied across the different methods, including probe length (also known as Range Gate Length), range settings, measurement accumulation time, angular resolutions and angular ranges.

https://doi.org/10.5194/wes-2026-94
Preprint. Discussion started: 11 June 2026

eawe european academy of wind energy
Open Access WIND ENERGY SCIENCE DISCUSSIONS

Table 2. Scanning lidar scan settings applied to the different methods during experiment.

Test & Scan type	Parameter	SL South	SL North
Static HTT (NOAH)	Probe length [m]	150	150
	Range resolution [m]	10	10
	Range min/max [m]	4500 / 6080	6000 / 7580
	Accumulation time [s]	0.1	0.1
	ϕ resolution [°]	0.01	0.01
	θ resolution [°]	0.01	0.01
Dynamic HTT (Drone)	Probe length [m]	25	150
	Range resolution [m]	1	50
	Range min/max [m]	350 / 668	3000 / 10900
	Accumulation time [s]	0.1	0.1
	ϕ_{lidar} resolution[°]	0.01	0.01
	θ_{lidar} resolution [°]	0.01	0.01
SSL	Probe length [m]	50	75
	Range resolution[m]	20	20
	Range min/max [m]	150 / 6510	150 / 6510
	Accumulation time [s]	0.1	0.1
SSL RHI	ϕ_{lidar} resolution [°]	0.02	0.02
	ϕ_{lidar} min/max [°]	-2 / $+1$	-2 / $+1$
	θ_{lidar}[°]*	34.60,69.60,104.60	129.25,164.25,199.25
SSL PPI	θ_{lidar} resolution [°]	0.1	0.1
	θ_{lidar}* min/max [°]	34.6 / 104.6	129.25 / 199.25
	ϕ_{lidar} [°]	-0.72,-0.15,0.30	-1.06,-0.46,0.00

*It is assumed that $\theta_{\text{lidar}} \simeq \theta_{\text{ref}}$ since a static azimuth offset is programmed in both devices.

https://doi.org/10.5194/wes-2026-94
Preprint. Discussion started: 11 June 2026

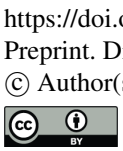

eawe european academy of wind energy
Open Access WIND ENERGY SCIENCE DISCUSSIONS

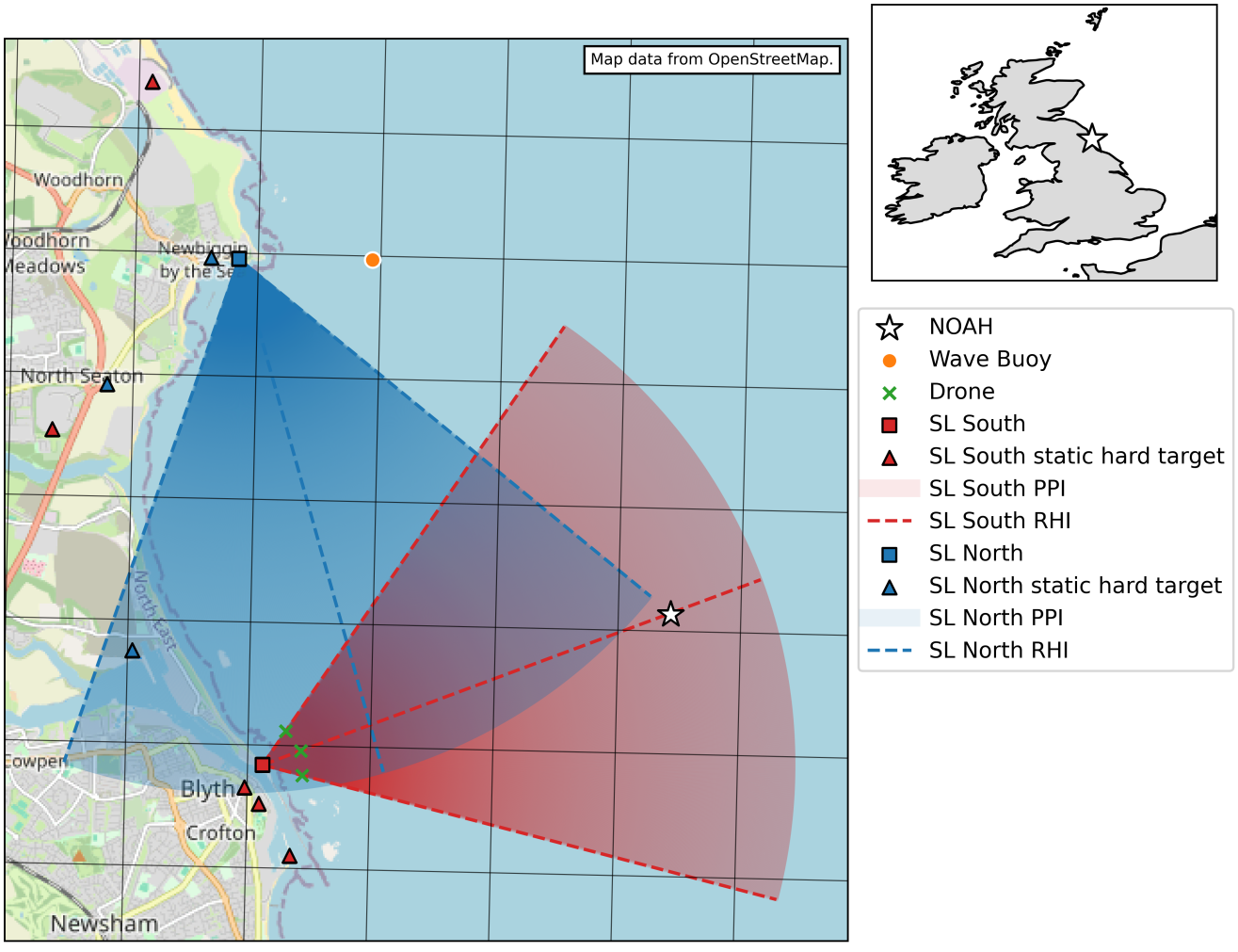

Figure 3. Map of experiment showing the locations of each lidar device, reference hard target target (NOAH met mast), static hard targets, drone, and sea surface scan geometry.

2.3.1 Static Hard Target

Viable SHT candidates were selected based on the available field of view at each site relative to suitable hard targets. This led to five viable target candidates for SL South and three for SL North. The targets comprise a mixture of building edges and masts with varying distances from the devices. The locations and heights of each static hard target were determined using the total station and are given in Table 3. Multiple PPI scans at consecutive elevation angles were used to build CNR maps of the area around each target. θ_{lidar} and ϕ_{lidar} for the target location were then obtained from the CNR maps and compared with θ_{ref} and ϕ_{ref} obtained from the total station measurements in Table 3.

https://doi.org/10.5194/wes-2026-94
Preprint. Discussion started: 11 June 2026

eawe european academy of wind energy
Open Access WIND ENERGY SCIENCE DISCUSSIONS

Table 3. Positions of NOAH, scanning lidar, static hard target candidates and drone flights determined from total station survey. For the scanning lidar the height corresponds to the height of the scanner head.

Name	ID	Longitude [°]	Latitude [°]	Height [m amsl]	Distance [m]
NOAH		-1.420867	55.14625	103.0	–
SL South		-1.4993	55.1297	10.14	5336.9*
SL North		-1.5038	55.1853	10.51	6830.0*
Static hard target SL South	S1	-1.4941	55.1198	32.8	1157.9
	S2	-1.5001	55.1255	29.3	475.4
	S3	-1.5028	55.1273	28.0	351.7
	S4	-1.5397	55.1666	45.4	4859.8
	S5	-1.5204	55.2047	120.7	8475.5
Static hard target SL North	N1	-1.5243	55.1423	47.4	4967.8
	N2	-1.5292	55.1716	58.4	2230.7
	N3	-1.5091	55.1854	17.2	338.0
Drone (Center/NOAH)	D1	-1.4919	55.1313	19.3, 16.1, 12.9	500.0
Drone (North)	D2	-1.4948	55.1334	19.3, 16.1, 12.9	500.0
Drone (South)	D3	-1.4917	55.1286	19.3, 16.1, 12.9	500.0

*Distance from each scanning lidar to NOAH

2.3.2 Dynamic Hard Target

The DHT method using the lidar beam to acquire the drone (i.e. drone acquisition as opposed to beam acquisition; Oldroyd et al. (2024)) has been implemented to align with the CNR-mapping approach of the SHT method. Like the SHT method, θ_{ref} and ϕ_{ref} are calculated using the positions (x,y,z) of the lidar and drone, whereas θ_{lidar} and ϕ_{lidar} are determined from the lidar CNR map obtained from scanning the drone in mid-flight.

A DJI Matrice 350 RTK drone was used for the experiment with horizontal and vertical dimensions of approximately 0.77 m and 0.43 m, respectively. Similar to Thorsen et al. (2023), a real-time kinematics (RTK) system was used to correct the position of the drone in real-time. This uses two D-GNSS antenna onboard on the drone, communicating with an RTK base station positioned next to the drone controller. The drone position during each flight was also independently measured using a total station, which was used to independently verify the drone position determined by the RTK. A reflective sticker was positioned on the upper front casing of the drone body to use as a reference point for total station measurements and lidar scans, ensuring the position of dominant CNR return.

A total of 8 independent drone flights were executed over a 4-day period next to SL South across a range of wind speed conditions (Table 4). Due to flight safety restrictions it was not possible to conduct the test at SL North. During each flight

https://doi.org/10.5194/wes-2026-94
Preprint. Discussion started: 11 June 2026

eawe european academy of wind energy
Open Access WIND ENERGY SCIENCE DISCUSSIONS

the drone was flown to one of three predetermined target locations 500m offshore from SL South (Table 3). Location D1 is placed along the approximate pointing azimuth of SL South to the NOAH reference of $\theta = 70°$, whereas locations D2 and D3 are $\theta \pm 35°$ to the north and south of D1. This approach was employed first to assess applying the DHT drone method at near-range to determine the beam position in the desired far-range campaign measurement location at NOAH, and second form an additional reference to assess the sinusoidal variation in ϕ_{off} as a function of θ against the SHT and SSL methodologies.

During a flight at a given location, the drone was flown at three different heights, 19.3 m (H1), 16.1 m (H2), 12.9 m (H3) above mean sea-level. These heights are equivalent to the elevation angle of a fixed lidar beam from SL South aimed at heights of approximately 108 m, 73 m and 40 m at the NOAH distance, each within 6 m of 103 m, 69 m and 35 m boom arms of the NOAH mast on which cup anemometers are placed.

During each day, the drone test procedure was:

1. Setup drone, RTK base station and total station at known locations.
2. Fly drone to target location at first height and hover.
3. Aim the total station at the reflective sticker to acquire drone position independently of RTK.
4. Scan drone using SL South (and where applicable SL North), starting with a fast $0.1°$ angular resolution scan to initially find the drone, followed by a $0.01°$ angular resolution scan to accurately determine the drone footprint.
5. Fly drone to next height and repeat steps 3. and 4.

Prior to the main flights to D1, D2 and D3, an initial test flight was performed at 250 m distance to determine general flight stability and the drone footprint in hard target mapping from the frame of reference of the lidar for different orientations of the drone. For all subsequent flights, the general procedure was to first fly to the highest height (19.3 m) and then lower the drone to the other two heights. During flights #4 and #6 this procedure was also followed by raising the drone back to the higher heights to test flight control sensitivity. While the primary aim during most flights was short-range drone acquisition at 500 m using SL South, long-range drone acquisition at 6 km was conducted using SL North during flights #7 and #8. Additionally, during flight #7, both the drone and the NOAH mast were simultaneously scanned by SL South to examine the short-range drone versus long-range static target footprints in hard target mapping.

Using the resulting lidar scan data of the drone at 500 m range, θ_{lidar} and ϕ_{lidar} were obtained from the position of the reflective sticker in the center of the drone body. As discussed in Section3.2 this was the area associated with highest CNR in the scan.

2.3.3 Sea Surface Leveling

A comprehensive overview of sea surface levelingmethodologies are given in Rott et al. (2022); Gramitzky et al. (2026). Both PPI and RHI type scan strategies can be used to intersect the sea surface, where the range of beam immersion is measured by a notable drop in CNR. In this experiment we apply and evaluate two implementations of the method for estimating ϕ_{off} at a coastal location as follows.

https://doi.org/10.5194/wes-2026-94
Preprint. Discussion started: 11 June 2026

eawe european academy of wind energy
Open Access WIND ENERGY SCIENCE DISCUSSIONS

Table 4. Summary of drone flights performed during the test. The wind speed is presented as the minimum, mean $\pm 1\sigma$ (standard devation), and maximum ambient wind speed measured by the drone. device 'S' or 'N' corresponds to SL South and SL North, respectively. PL corresponds to Probe Length, N Acq. is the total number of acquisitions of the drone made by the lidar, and the number at each height level for a given flight are given in columns H1 (19.3 m), H2 (16.1 m) and H3 (12.9 m).

Flight #	Location	Date/Time start	Duration [min]	Wind speed [m s^{-1}]	Device	PL[m]	N Acq.	H1	H2	H3
1	D1	23/4/2025 09:22	33	$5.7, 6.6 \pm 0.3, 7.3$	S	25	4	1	1	2
2	D2	23/4/2025 10:19	23	$4.1, 5.4 \pm 0.8, 7.6$	S	25	3	1	1	1
3	D3	23/4/2025 11:11	13	$5.5, 6.5 \pm 0.2, 6.9$	S	25	3	1	1	1
4	D1	24/4/2025 10:07	31	$4.0, 4.6 \pm 0.2, 5.0$	S	100	3	1	1	1
5	D2	24/4/2025 11:07	16	$4.4, 5.1 \pm 0.2, 5.4$	S	25	3	1	1	1
6	D3	24/4/2025 11:38	15	$5.1, 5.8 \pm 0.2, 6.2$	S	25	3	1	1	1
7	D1	28/4/2025 10:24	28	$5.8, 9.3 \pm 1.7, 13.1$	S, N	150	6	6	-	-
8	D1	28/4/2025 11:03	12	$4.1, 7.6 \pm 1.7, 10.6$	S, N	150	2	2	-	-

Using a PPI or RHI scan to determine the sea surface range r_{ss} and therefore the relative height of the lidar above sea level h_{lidar}, ϕ_{ref} can be calculated via

$$\phi_{\text{ref}} = -\arcsin\left(\frac{h_{\text{lidar,sea}}}{r_{\text{ss}}}\right) \tag{4}$$

with

$$h_{\text{lidar,sea}} = h_{\text{lidar,amsl}} - h_{\text{tide}} + h_{\text{curve}} \tag{5}$$

where, $h_{\text{lidar,amsl}}$ is the height of the lidar above mean sea level (amsl), h_{tide} the relative tidal height with respect to mean sea level and h_{curve} is the relative change in height of the surface due to the drop in curvature of the Earth with distance (see Fig.2). We approximate h_{curve} using

$$h_{\text{curve}} \approx \frac{r_{\text{ss}}^2}{2r_e} \tag{6}$$

where the radius of the Earth r_e is 6371 km, and based on the assumption that $r_{\text{ss}} \approx$ horizontal distance when $h_{\text{lidar,sea}} << r_{\text{ss}}$ (Gramitzky et al., 2026). Thus, this approach requires prior knowledge of only $h_{\text{lidar,amsl}}$ and h_{tide}, in addition to r_{ss} determined from the sea surface scan. By combining equations 2, 4, 5 and 6, and defining the effective lidar height as $h_{\text{eff}} = h_{\text{lidar,amsl}} - h_{\text{tide}}$, ϕ_{off} can be estimated via

$$\phi_{\text{off}}(\phi_{\text{lidar}}, h_{\text{eff}}, r_{\text{ss}}) = \phi_{\text{lidar}} - \left(-\arcsin\left(\frac{h_{\text{eff}} + \frac{r_{\text{ss}}^2}{2r_e}}{r_{\text{ss}}}\right)\right) \tag{7}$$

https://doi.org/10.5194/wes-2026-94
Preprint. Discussion started: 11 June 2026

eawe european academy of wind energy
Open Access WIND ENERGY SCIENCE DISCUSSIONS

This approach is denoted as the SSL method.

Alongside the SSL method, we apply the simplified extended SSL method (Ext. SSL) proposed by Gramitzky et al. (2026). The method defines ϕ_{lidar} as a function of device tilt, elevation offset, sea surface range and lidar height, applying small angle approximations to simplify the formulation such that

$$\phi_{\text{lidar}} = \alpha\cos(\theta_{\text{lidar}}) - \beta\sin(\theta_{\text{lidar}}) - \frac{h_{\text{eff}} - \frac{r_{\text{ss}}^2}{2r_e}}{r_{\text{ss}}} - \phi_{\text{off}} \tag{8}$$

where α is the pitch (north-south tilt) and β is the roll (east-west tilt) of the lidar device. Thus the Ext. SSL method differs from the SSL method by incorporating device tilt. Using multiple measurements of r_{ss}, at different ϕ_{lidar} , θ_{lidar}, from RHI or PPI scans, Gramitzky et al. (2026) use a non-linear least squares curve fitting approach to estimate α, β, h_{eff} and ϕ_{off}. We also apply this approach constraining the parameters to physically realistic ranges of $-0.05° \leq \alpha/\beta \leq 0.05°$, 5 m $\leq h_{\text{eff}} \leq$ 15 m, and $-0.5° \leq \phi_{\text{off}} \leq 0.5°$ to minimise errors of the estimated parameters. Furthermore, to reduce the number of unknown variables in Eq. (8) to be estimated from the curve fit, we also apply the method using the device inclinometer measurements of α and β, in addition to r_{ss}, ϕ_{lidar} and θ_{lidar}, thus estimating only the two unknowns: h_{eff} and ϕ_{off}. Note that for Eq. (8), Gramitzky et al. (2026) define ϕ_{off} as $\phi_{\text{ref}} - \phi_{\text{lidar}}$, which is the reverse of Eq. (2) and therefore the resulting ϕ_{off} estimated using Eq. (8) is multiplied by -1 to yield ϕ_{off} in the same convention as the other methods. We also only apply the Ext. SSL method to RHI scans as the PPI scans were not performed across enough elevation angles to obtain reliable estimates of the offset at a given azimuth angle from the curve fit.

An inverse sigmoid function is suitable for describing the CNR behavior with range from a sea surface intersecting scan and thus determine r_{ss} (Rott et al., 2022). However, at longer sea surface ranges and thus smaller scan elevation angles, the natural attenuation of CNR with range prior to the beam hitting the sea poses an ill-fitting signal for the standard inverse sigmoid (Gramitzky et al., 2024). Instead Gramitzky et al. (2024) suggest to account for this by using a modified sigmoid of the following form with a decay factor

$$\text{CNR}(d) = \frac{(\text{CNR}_{\text{high}} - \text{CNR}_{\text{low}}) \cdot (1 + A \cdot (d - i_p))}{1 + \exp((d - i_{\text{p}}) \cdot g)} + \text{CNR}_{\text{low}} \tag{9}$$

where CNR_{high} and CNR_{low} are the high and low values of inverse sigmoid, d is the distance from the lidar (i.e. range), g is the growth rate of the function, A is a constant defining the CNR variation with range before water intersection, and i_p is the inflection point, i.e., the range that the beam hits the sea surface, r_{ss}. r_{ss} is therefore estimated by fitting the function to the CNR data with range using least squares. For the pulsed lidar devices used in this study, due to the relatively long probe length (25 m to 75 m) over which the lidar return signal is averaged alongside the sharp reduction in logarithmic CNR identified at i_p, it is expected that i_p is more representative of the distance of an immersed pulse rather than the distance of the water surface and therefore needs reduced to determine r_{ss} (Gramitzky et al., 2026). We therefore apply a constant distance correction to i_p such that $r_{\text{ss}} = i_p - 1/2$ probe length as proposed by Gramitzky et al. (2026), assuming that the range of each measurement is representative of the center of the probe volume. The impact of this correction is shown in Section 3.3.

In this experiment, the SSL method is implemented using r_{ss} determined from both PPI and RHI scans to evaluate the results from these two different scan strategies. PPI scans are executed across an azimuthal arc range of 75° at three ϕ_{lidar}, intersecting

https://doi.org/10.5194/wes-2026-94
Preprint. Discussion started: 11 June 2026

eawe european academy of wind energy
Open Access WIND ENERGY SCIENCE DISCUSSIONS

mean sea level at ranges of approximately 500 m, 1000 m and 4500 m from each device (Table 2). While PPI scan results from all three ϕ_{lidar} are presented for SL North, only those from the first two elevation angles are presented for SL South as the PPI scans at the highest elevation angle infrequently intersected the sea surface and thus yielded poor results. Similarly, three RHI scans are executed at the first, middle and last azimuth of the PPI scans starting from $\phi_{\text{lidar}} = -2°$ to $\phi_{\text{lidar}} = -1°$ (Table 2). Therefore the PPI scans determine variations of ϕ_{off} with azimuth, whereas the RHI scans determine variations in ϕ_{off} with elevation, with both scan types intersecting for comparison at three equivalent azimuths and elevation angles. For intercomparison, the azimuths of the SSL scans at SL South are aligned with the locations of the drone and NOAH, whereas at SL North the first azimuth is aligned with NOAH and limited to the southern directions to avoid beam occlusion due to local buildings located to the east and north of the device (Fig. 3). The PPI and RHI scans were performed consecutively in a continuous cycle (i.e. sequence: PPI_{ϕ_1}, PPI_{ϕ_2}, PPI_{ϕ_3}, RHI_{θ_1}, RHI_{θ_2}, RHI_{θ_3}) during 29 – 30 April 2025. By recommendation from the lidar manufacturer, additional redundant fixed beam scans of 1 s duration with angular offsets of $-0.5°$ for SL South and $-0.1°$ for SL North applied to the initial θ_{lidar} and ϕ_{lidar} of each scan were programmed between each PPI and RHI scan to minimise the effect of mechanical backlash on the pointing stability of the respective scanner heads during the test. The magnitudes of the angular offsets applied to each device differed due to the different scan head mechanisms of each device (Table 1).

For each SSL scan type, the CNR versus range measurements at each combination of θ_{lidar} and ϕ_{lidar} are aggregated every 15 min to match the temporal frequency of the nearest tidal gauge measurements at North Shields. This temporal aggregation approach leads to an estimated value of r_{ss} and ϕ_{off} every 15-min for every combination of θ_{lidar} and ϕ_{lidar} for the SSL method, and a single estimate of ϕ_{off} every 15-min for the Extended SSL method. To help prevent over-fitting, increase the likelihood of a good fit, and computationally optimise the curve-fit procedure, the temporally aggregated CNR measurements are min/max normalised to fall between 0 and 1 via

$$CNR_{norm} = \frac{CNR - min(CNR)}{max(CNR) - min(CNR)} \tag{10}$$

We examined the sensitivity of the modified sigmoid (Eq. 9) curve fitting results using the non-normalised standard CNR versus the min/max normalised data, and found similar results. The resulting curve fits are filtered for goodness of fit by applying a threshold of > 0.8 to the r-squared of the resulting curve fits versus the original data, and requiring that the standard deviation derived from the r_{ss} variance of the curve fit falls within the scan range resolution of 20m. The distributions of these parameters alongside the resulting r_{ss} and ϕ_{off} are shown in Section 3.3.

2.4 Uncertainty Quantification

A summary of the uncertainty components used across the different hard targeting methods is given in Table 5. Based on Eq. (2), the total uncertainty in the elevation offset $u_{\phi_{\text{off}}}$ derived from each hard targeting method can be expressed as the quadrature sum of the uncertainties $u_{\phi_{\text{ref}}}$ and $u_{\phi_{\text{lidar}}}$. For the SHT method, due to the very high accuracy of the total station device used to determine ϕ_{ref}, it can be assumed that $u_{\phi_{\text{ref}}}$ is negligible (Table 5). For example, scaling the total station error of ± 0.019 m to $u_{\phi_{\text{ref}}}$ [°] per static hard target using $\tan^{-1}(\frac{u_{\phi_{\text{ref}}}}{d})$ where d is the distance from the lidar to each target, yields very

https://doi.org/10.5194/wes-2026-94
Preprint. Discussion started: 11 June 2026

eawe european academy of wind energy
Open Access WIND ENERGY SCIENCE DISCUSSIONS

Table 5. Uncertainty components for hard target methods.

Method	Uncertainty term u	Value	Justification
SHT	$u_{\phi_{\text{ref}}}$	0°	Assumed negligible when converting total station vertical setting error ± 0.019 m plus manufacturers station calibration uncertainty of ± 0.002 m to ϕ.
DHT	$u_{\phi_{\text{ref}}}$	0.013°	Uncertainty in drone RTK positioning estimated as ± 0.113 m at 500 m comprising the following added in quadrature – hover stability standard deviation of drone RTK coordinates during hovering across all flights: ± 0.1 m; – RTK positioning error: manufacturer specification: ± 0.015 m; – RTK base station position error: ± 0.05 m.
SHT/DHT	u_{sys}	0.03°	Pixel picking confidence level
DHT	$\sigma_{\phi_{\text{off}}}$	-	Standard deviation of ϕ_{off} from multiple scans
SSL	$u_{\phi_{\text{lidar}}}$	0.02°	Angular resolution (step) of RHI scans
SSL	$u_{h_{\text{lidar,amsl}}}$	0.1 m	Measured using GNSS antenna with an accuracy of 0.06m rounded to nearest 0.1m.
SSL	$u_{h_{\text{tide}}}$	0.5 m	The maximum change in tidal height between consecutive 15-min measurements of 0.4 m plus an additional tolerance of 0.1 m accounting for spatial variations along the coast due to distance from tidal gauge.
SSL	$u_{h_{\text{eff}}}$	0.51 m	Effective lidar height (h_{eff}) uncertainty $= \sqrt{u^2_{h_{\text{lidar,amsl}}} + u^2_{h_{\text{tide}}}}$
SSL	$u_{r_{\text{ss}}}$	20 m	Set to the range resolution of scans.

small values of $u_{\phi_{\text{ref}}} = 3.9^\circ \times 10^{-8}$ at longest target distance of 8475.5m to $u_{\phi_{\text{ref}}} = 9.8^\circ \times 10^{-7}$ at shortest target distance of 338.0 m. Therefore, $u_{\phi_{\text{off}}}$ is dominated by $u_{\phi_{\text{lidar}}}$. In general, $u_{\phi_{\text{lidar}}}$ is dependent on the stability of the scanner head, driven by temporal variability of the external lidar levels and the internal alignment of the scanner head. We therefore define $u_{\phi_{\text{off}}}$ as a combination of random and systematic uncertainties such that

$$u_{\phi_{\text{off}}} = \sqrt{u^2_{\phi_{\text{lidar,rand}}} + u^2_{\phi_{\text{lidar,sys}}} + u^2_{\phi_{\text{ref}}}} = \sqrt{\frac{\sigma^2_{\phi_{\text{lidar,rand}}}}{N} + u^2_{\phi_{\text{lidar,sys}}} + u^2_{\phi_{\text{ref}}}} \tag{11}$$

where $\sigma_{\phi_{\text{lidar,rand}}}$ the sample standard deviation of ϕ_{lidar} obtained across N repeated measurements (i.e. random component), and $u_{\phi_{\text{lidar,sys}}}$ is a systematic uncertainty. Using hard targeting, $\sigma_{\phi_{\text{lidar,rand}}}$ is estimated by repeating scans over the same target and determining ϕ_{lidar} from the target location each time.

https://doi.org/10.5194/wes-2026-94
Preprint. Discussion started: 11 June 2026

eawe european academy of wind energy
Open Access WIND ENERGY SCIENCE DISCUSSIONS

For the SHT and DHT methods, we assume $u_{\phi_{\text{lidar,sys}}}$ primarily originates from ambiguities in determining the exact hard target position from the CNR map and set $u_{\phi_{\text{lidar,sys}}} = 0.03°$. This is a conservative value 3 times the $0.01°$ angular resolution of the SHT scans (Table 2), discussed in Section 3.1. We found that for temporally consecutive scans of the same static hard target, ϕ_{lidar} was constant. Therefore, assuming $\sigma_{\phi_{\text{lidar,rand}}} \approx 0°$ we obtain $u_{\phi_{\text{off}}} = \sqrt{u^2_{\phi_{\text{lidar,sys}}} + u^2_{\phi_{\text{ref}}}} = 0.03°$. However, scans of the reference static hard target (NOAH) conducted on different days by SL South exhibited small variations in ϕ_{lidar} where $\sigma_{\phi_{\text{lidar,rand}}} = 0.01°$. Accounting for this for this specific static target and lidar still led to $u_{\phi_{\text{off}}} \approx 0.03°$ due to the dominant contribution from $u_{\phi_{\text{lidar,sys}}}$ to the total uncertainty.

A Monte Carlo approach is used to extrapolate ϕ_{off} with associated standard error $u_{\phi_{\text{off}}}$ across the full azimuthal range of $0° \leq \theta_{\text{lidar}} \leq 360°$ and thus estimate ϕ_{off} in the reference pointing direction using the static hard target candidates (Champneys et al., 2024). The Monte Carlo method is applied by deriving a normal distribution per available hard target using ϕ_{off} as the mean and $u_{\phi_{\text{off}}}$ as the standard deviation. The distributions from all available hard target points are then randomly sampled together 50,000 times and the sinusoidal function in Eq. (3) is fitted to the sampled points each time. The per azimuth ϕ_{off} mean and standard deviation of the 50,000 sinusoid are then used to determine ϕ_{off} and its associated standard error in the desired azimuthal direction.

Since the DHT method uses a non-static hard target, we determine $u_{\phi_{\text{off}}}$ via

$$u_{\phi_{\text{off}}} = \sqrt{\frac{\sigma^2_{\phi_{\text{off}}}}{N} + u^2_{\phi_{\text{lidar,sys}}} + u^2_{\phi_{\text{ref}}}} \tag{12}$$

where, $\sigma_{\phi_{\text{off}}}$ is the sample standard deviation of ϕ_{off} determined from N independent hard target scans of the drone and $u_{\phi_{\text{lidar,sys}}} = 0.03°$, the same as the SHT method. $u_{\phi_{\text{ref}}}$ is made up of the drone hover stability (standard deviation of drone RTK coordinates during hovering across all flights ± 0.1 m), RTK positioning error (manufacturer specification ± 0.015 m), and RTK base station position error (± 0.05 m) added in quadrature to give a total error of ± 0.113 m corresponding to $u_{\phi_{\text{ref}}} = 0.013°$ at 500 m range (Table 5).

For the SSL method, noting that h_{curve} is a function of ϕ_{lidar} and r_{ss} (from Eq. (6)), the uncertainty $u_{\phi_{\text{off}}}$ determined at ϕ_{lidar} from a single sea surface measurement, i, can be derived by applying partial derivatives to Eq. (7), such that

$$u^2_{\phi_{\text{off}},i} = \left(\frac{\partial \phi_{\text{off,i}}}{\partial \phi_{\text{lidar,i}}} u_{\phi_{\text{lidar}}}\right)^2 + \left(\frac{\partial \phi_{\text{off,i}}}{\partial h_{\text{eff}}} u_{h_{\text{eff}}}\right)^2 + \left(\frac{\partial \phi_{\text{off,i}}}{\partial r_{\text{ss,i}}} u_{r_{\text{ss}}}\right)^2 \tag{13}$$

where each u term is a constant uncertainty associated with each variable given in Table 5 and the uncertainty components are assumed uncorrelated. The partial derivative components can be expressed as:

$$\frac{\partial \phi_{\text{off,i}}}{\partial \phi_{\text{lidar,i}}} = 1 \tag{14}$$

$$\frac{\partial \phi_{\text{off,i}}}{\partial h_{\text{eff}}} = \frac{1}{r_{\text{ss,i}} \sqrt{1 - \left(\frac{h_{\text{eff}} + \frac{r^2_{\text{ss}}}{2r_e}}{r_{\text{ss,i}}}\right)^2}} \tag{15}$$

https://doi.org/10.5194/wes-2026-94
Preprint. Discussion started: 11 June 2026

eawe european academy of wind energy
Open Access WIND ENERGY SCIENCE DISCUSSIONS

$$\frac{\partial \phi_{\text{off,i}}}{\partial r_{\text{ss,i}}} = \frac{-\frac{h_{\text{eff}}}{r_{\text{ss}}^2} + \frac{1}{2r_e}}{\sqrt{1 - (\frac{h_{\text{eff}} + \frac{r_{\text{ss}}^2}{2r_e}}{r_{\text{ss,i}}})^2}} \tag{16}$$

We calculate the mean and maximum $u_{\phi_{\text{off}}}$ estimated for the SSL method from the above equations throughout the SSL test, to obtain an average and conservative uncertainty estimate. For the Extended SSL method we attribute the analytical uncertainty $u_{\phi_{\text{off}}}$ to the standard error of ϕ_{off} estimated from covariance matrix of the curve fit. The mean and maximum value is reported.

3 Results

This section presents detailed results from the SHT, DHT and SSL methods, followed by an intercomparison of the different methods presented in Section 3.4.

3.1 Static Hard Target

Figures 4 and 5 show the resulting CNR maps for SL South and SL North, respectively, for each of the static hard target candidates which have been used to determine θ_{lidar} and ϕ_{lidar} and obtain θ_{off} and ϕ_{off} presented in Table 6. The CNR distributions differ among the hard target structures, depending on the shape, size, orientation and range of each target with respect to the lidar and angular resolution ($0.01°$) of the hard target scans. Due to the natural decay of CNR as a function of increasing range from the device, near-range targets are associated with high positive CNR values (+5 dB to >+20 dB), whereas far-range targets above 5000 m may exhibit near-zero and slightly negative CNR values. The varying shape and structure of each target highlights the challenge of identifying the pixel corresponding to the exact target point for calibration from the CNR map. This so-called "pixel picking error" is accounted for by the systematic error of 0.03° per scan in the uncertainty quantification (see Section 2.4).

For the NOAH reference hard target, the side mounted boom arms on which cup anemometers are placed at 103 m and 86 m can be delineated from the CNR maps derived from both lidars (Fig. 4 and 5). The elevation angle difference between these boom arms is approximately $0.19°$ for SL South and $0.15°$ for SL North which is equivalent to vertical height variations of 17.6 m and 17.9 m, respectively. Although these height variations are within 1 m of the expected 17 m height difference between the boom arms, they are not exactly equal to 17 m due to ambiguity in determining the correct target pixel, which is more pronounced for longer range targets. This is highlighted across the variety of target candidate ranges used; for the same $0.01°$ angular resolution of each scan, a horizontal and vertical distance of 1 m in the CNR map corresponds to a larger angular variation for near range targets compared to far range targets (e.g. several pixels at near range but only a few pixels at far range). Therefore the precise target position is easier to distinguish from near range targets.

Figures 6 presents $\phi_{\text{off}} \pm u_{\phi_{\text{off}}}$ as a function of azimuth for each of the SHT candidates, with $u_{\phi_{\text{off}}} = 0.03°$. Across all targets including NOAH, the range between minimum and maximum ϕ_{off} is $0.23°$ for SL South and $0.07°$ for SL North (Table 6). For

https://doi.org/10.5194/wes-2026-94
Preprint. Discussion started: 11 June 2026

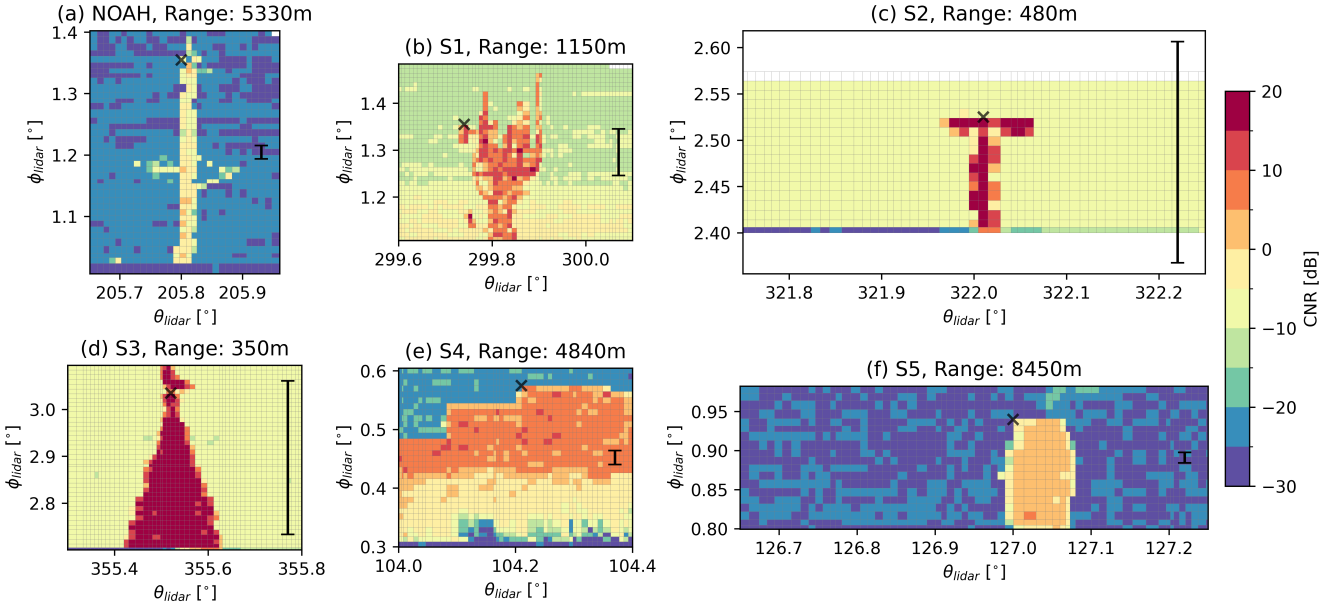

Figure 4. Static Hard Target measurements from SL South showing CNR as a function of local lidar azimuth, θ_{lidar} and elevation, ϕ_{lidar} angles across the different SHT candidates. Black crosses indicate the target point used for calibration whereas the black scale bars represent the equivalent vertical/horizontal distance of 1m at each target range. Each map is derived from scans with an angular resolution in θ_{lidar} and ϕ_{lidar} of 0.01°.

Table 6. Summary of static hard target results determined for SL South and SL North, where NOAH was used as the reference target for both devices. It is to be noted that the test performed on SL South, using NOAH as the target (first row), had 16 repetitions (N = 16) yielding $\sigma_{\phi_{\text{off}}} = 0.01°$. The other tests are standardised to one repetition, hence no standard deviation is defined.

Lidar	Target	N	Distance [m]	Range [m]	θ_{ref} [°]	θ_{lidar}[°]	θ_{off} [°]	ϕ_{ref} [°]	ϕ_{lidar} [°]	ϕ_{off} [°]	u_{off} [°]
SL South	Ref. (NOAH)	16	5336.87	5337.64	69.60	205.80	136.20	0.97	1.35	0.38	0.03
	S1	1	1157.93	1158.15	162.19	299.75	137.55	1.12	1.36	0.24	0.03
	S2	1	475.36	475.74	185.74	322.01	136.27	2.31	2.53	0.22	0.03
	S3	1	351.71	352.16	219.24	355.52	136.28	2.90	3.05	0.15	0.03
	S4	1	4859.81	4859.93	326.78	104.21	137.43	0.39	0.58	0.19	0.03
	S5	1	8475.46	8476.11	349.61	127.00	137.39	0.71	0.95	0.24	0.03
SL North	Ref. (NOAH)	1	6830.03	6830.61	129.25	175.62	46.37	0.75	0.88	0.13	0.03
	N1	1	4967.82	4967.95	194.87	242.46	47.59	0.40	0.55	0.15	0.03
	N2	1	2230.68	2231.19	225.56	273.09	47.53	1.22	1.42	0.20	0.03
	N3	1	337.95	338.02	272.90	319.29	46.39	1.13	1.30	0.17	0.03

https://doi.org/10.5194/wes-2026-94
Preprint. Discussion started: 11 June 2026

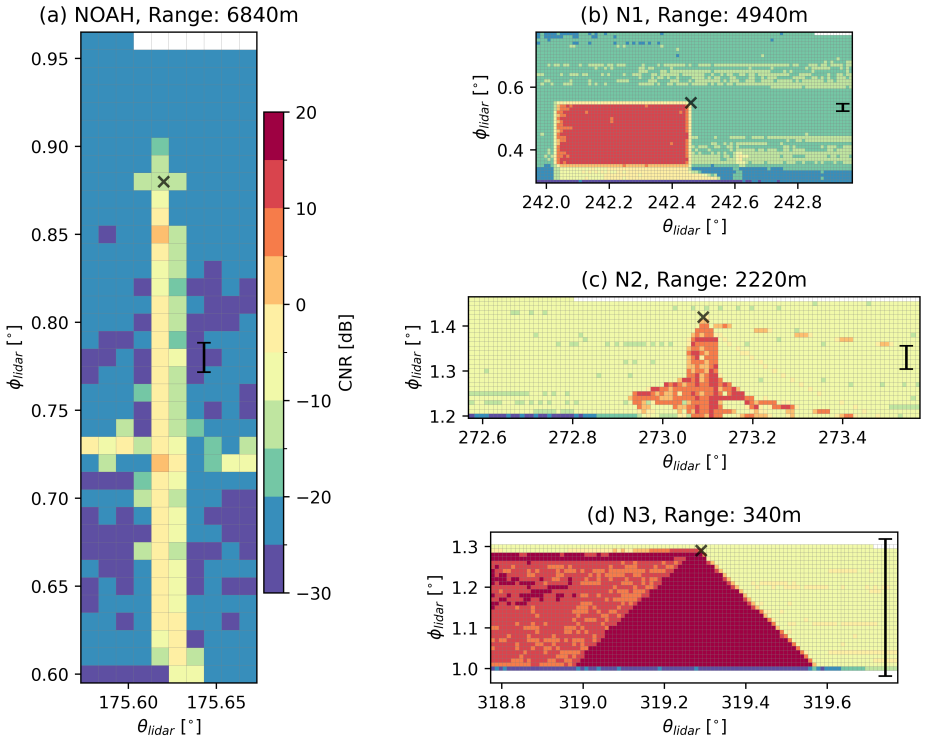

Figure 5. As Figure 4 but for SL North.

each lidar, a least-squares fit has been applied to ϕ_{off} from all SHT measurements except the NOAH reference to determine the sinusoidal function (Eq. 3) . Comparing the results from the two devices shows that the suitability of using the sinusoid to extrapolate ϕ_{off} across the full azimuthal range highly depends on the distribution (location and separation) and number of available SHT candidates. For SL South, the 5 candidates span an azimuth range of $251°$and are distributed either side of the reference target (NOAH) positioned at the peak of the sinusoid. In contrast, the 3 candidates available for SL North are located across a smaller azimuth range of $77°$ around the estimated peak of the sinusoid. These azimuthal distributions lead to very different sinusoidal predictions of ϕ_{off} in the desired reference pointing direction of NOAH with a difference relative to the reference ϕ_{off} of $-0.03°$ for SL South and $-0.2°$ for SL North which would lead to respective pointing height errors of 2.8 m and 23.8 m at the NOAH range.

The under-prediction highlights the practical limitations of the SHT sinusoid method to estimate ϕ_{off} in the desired pointing direction particularly if there is small azimuthal spacing between targets, a limited field of view for the lidar and/or availability of suitable target candidates. One recommendation is to have at least three targets each separated by at least $90°$ (Champneys et al., 2024).

https://doi.org/10.5194/wes-2026-94
Preprint. Discussion started: 11 June 2026

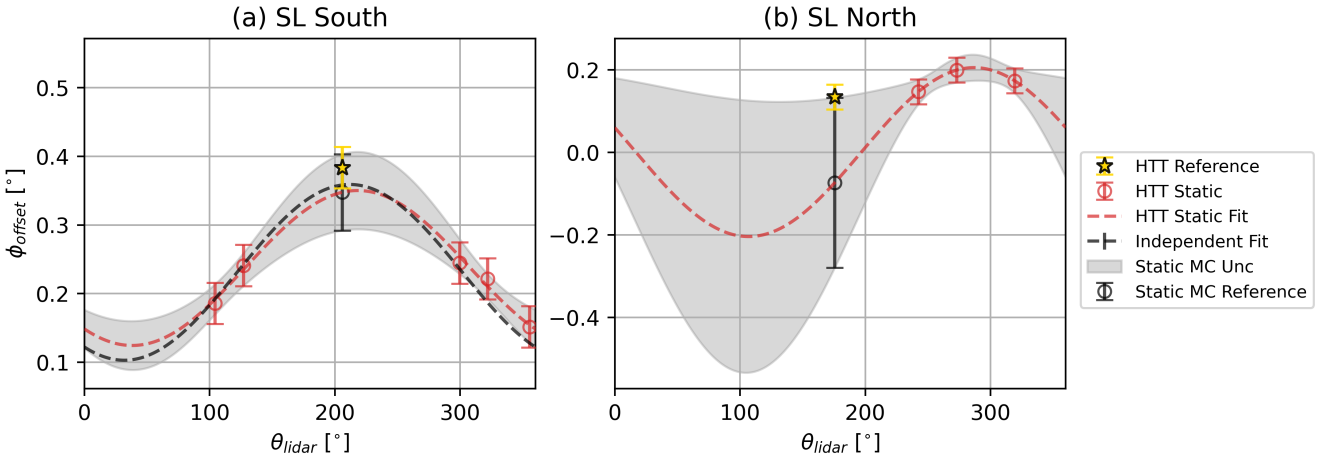

Figure 6. Elevation offset ϕ_{off} as a function of lidar azimuth θ_{lidar} for (a) SL South and (b) SL North from static hard target candidates. Error bars and shading indicate the standard uncertainty, u_{off}. The parameters obtained from the HTT static curve fit using Eq. (3) are $A = -0.11°$, $P = 51.90°$ and $O = 0.24°$ for SL South and $A = -0.21°$, $P = -16.81°$ and $O = 0.00°$ for SL North. The independent fit for SL South is the curve fit independently found for the device prior to deployment, by the manufacturer with parameters $A = -0.13°$, $P = 58.17°$ and $O = 0.23°$. An independent fit was not available for SL North.

3.2 Dynamic Hard Target

A summary of the hard target results obtained from the drone flights at D1, D2 and D3 locations is given in Table 7. Flights to location D1, in the reference hard target direction (NOAH) resulted in the largest number of drone acquisitions across all heights, whereas a total of 6 acquisitions each were obtained at locations D2 and D3. The mean CNR values of the drone target point obtained across all acquisitions ranged between 25.5 dB and 26.3 dB.

The standard deviations of the reference azimuth, $\sigma_{\theta_{\text{ref}}}$ and reference elevation, $\sigma_{\phi_{\text{ref}}}$ provide an indication of the horizontal and vertical positioning stability of the drone at each flight location/height across all flights. Stability in the horizontal position of the drone via $\sigma_{\theta_{\text{ref}}}$ was within $0.2°$ across all heights, equivalent to 2 m at 500 m range. Stability in the vertical position via $\sigma_{\phi_{\text{ref}}}$ was within $0.01°$ equivalent to 0.1 m at 500 m range, with the exception of location D3 at 103 m where $\sigma_{\phi_{\text{ref}}} = 0.04°$ and thus 0.35m at 500 m range. Although the drone position is by nature not completely static, the continual positioning recorded by the RTK system means that the drone position relative to the lidar was always known even if the position of the drone moved slightly at a given location/height during a flight or between flights. Consequently, variations in the azimuth and elevation offsets as given by $\sigma_{\theta_{\text{off}}}$ and $\sigma_{\phi_{\text{off}}}$ are typically smaller than $\sigma_{\theta_{\text{ref}}}$ and $\sigma_{\phi_{\text{ref}}}$. Overall, $\sigma_{\phi_{\text{off}}}$ was within $0.02°$ across all locations for all heights, with an overall uncertainty $u_{\phi_{\text{off}}}$ of $0.03°$.

Examples of different hard target scan results obtained during the drone test presented in the form of CNR maps are shown in Figure 8. The maps from an initial test flight at 250 m range show that the lidar is able to distinguish in detail the main features of the drone, including feet, wings, central body and GNSS antenna (top left), at close range (250 m) for different

https://doi.org/10.5194/wes-2026-94
Preprint. Discussion started: 11 June 2026

eawe european academy of wind energy
Open Access WIND ENERGY SCIENCE DISCUSSIONS

Table 7. Summary of drone-based hard target results determined for SL South, stratified by flight location and height. Each row corresponds to either mean values for distance, range, CNR, θ, ϕ, or the equivalent standard deviation σ derived from N independent drone acquisitions at each location/height. $u_{\phi_{off}}$ is the resulting uncertainty in ϕ_{off}.

Location	D1				D2				D3			
Height	All	35	69	103	All	35	69	103	All	35	69	103
N	15	3	2	10	6	2	2	2	6	2	2	2
Dist. [m]	500.37	501.75	500.75	499.88	501.23	501.28	500.93	501.49	501.27	501.90	500.77	501.15
Range [m]	500.44	501.76	500.79	499.97	501.28	501.29	500.97	501.57	501.31	501.90	500.81	501.22
CNR [dB]	26.09	25.64	25.74	26.30	25.51	25.51	25.56	25.46	25.56	25.53	25.58	25.59
θ_{ref}	69.662	69.786	69.752	69.606	34.780	34.843	34.761	34.735	104.758	104.750	104.765	104.759
$\sigma_{\theta_{\text{ref}}}$	0.108	0.009	0.026	0.088	0.099	0.057	0.043	0.177	0.014	0.003	0.019	0.019
θ_{lidar}	69.830	70.036	70.026	69.730	34.997	35.002	35.013	34.978	104.988	104.992	104.991	104.983
$\sigma_{\theta_{\text{lidar}}}$	0.196	0.007	0.030	0.161	0.105	0.016	0.016	0.230	0.018	0.004	0.008	0.038
θ_{off}	0.169	0.250	0.274	0.123	0.218	0.159	0.252	0.242	0.230	0.241	0.225	0.224
$\sigma_{\theta_{\text{off}}}$	0.090	0.004	0.057	0.074	0.063	0.073	0.028	0.053	0.013	0.007	0.011	0.019
ϕ_{ref}	0.855	0.315	0.684	1.052	0.677	0.316	0.679	1.037		0.316	0.681	1.006
$\sigma_{\phi_{\text{ref}}}$		0.001	0.009	0.007		0.006	0.011	0.001		0.000	0.004	0.037
ϕ_{lidar}		0.713	1.085	1.432		0.679	1.030	1.398		0.708	1.066	1.398
$\sigma_{\phi_{\text{lidar}}}$		0.003	0.001	0.008		0.018	0.011	0.004		0.023	0.017	0.049
ϕ_{off}	0.386	0.398	0.401	0.380	0.358	0.363	0.350	0.361	0.389	0.391	0.385	0.392
$\sigma_{\phi_{\text{off}}}$	0.012	0.002	0.011	0.009	0.008	0.012	0.000	0.003	0.015	0.023	0.021	0.012
$u_{\phi_{off}}$	0.030	0.030	0.031	0.030	0.030	0.031	0.030	0.030	0.031	0.034	0.033	0.031

orientations. The reflective sticker used as a reference point on the main body corresponds to the area of high CNR in the upper middle of the drone body (Fig. 8a,b), whilst it is obscured when the drone is positioned sideways relative to the lidar (Fig. 8c). Consequently, the drone was always orientated facing towards the device for all subsequent flights as shown in Fig. 8a. At 250 m range, the number of $0.01°$ pixels from the foot to the top of the drone is approximately 10 to 11 equivalent to 0.44 m to 0.48 m, in close agreement with the vertical dimension of the drone of 0.43 m. Similarly at 500 m range, the drone vertically spans $5 \times 0.01°$ pixels equivalent to 0.44 m and thus the 0.43 m vertical extent of the drone (Fig. 8e)

To compare the short-range drone acquisition and long-range static hard target procedure, both the drone and NOAH mast were simultaneously scanned within the same field of view by SL South during Flight #9 (Fig. 8d,e). From this single scan, the obtained elevation offsets from the drone and NOAH are within $0.003°$; with $\phi_{\text{off}} = 0.374°$ from the drone (using the RTK position as reference) and $\phi_{\text{off}} = 0.377°$ from the NOAH mast (using the total station survey as reference), illustrating the possibility of using the drone with RTK in replacement of a static hard target and complete hard target survey using a total station. During the same flight, the drone was also acquired at a range of 6km by SL North (Fig. 8f). At this distance, the drone

https://doi.org/10.5194/wes-2026-94
Preprint. Discussion started: 11 June 2026

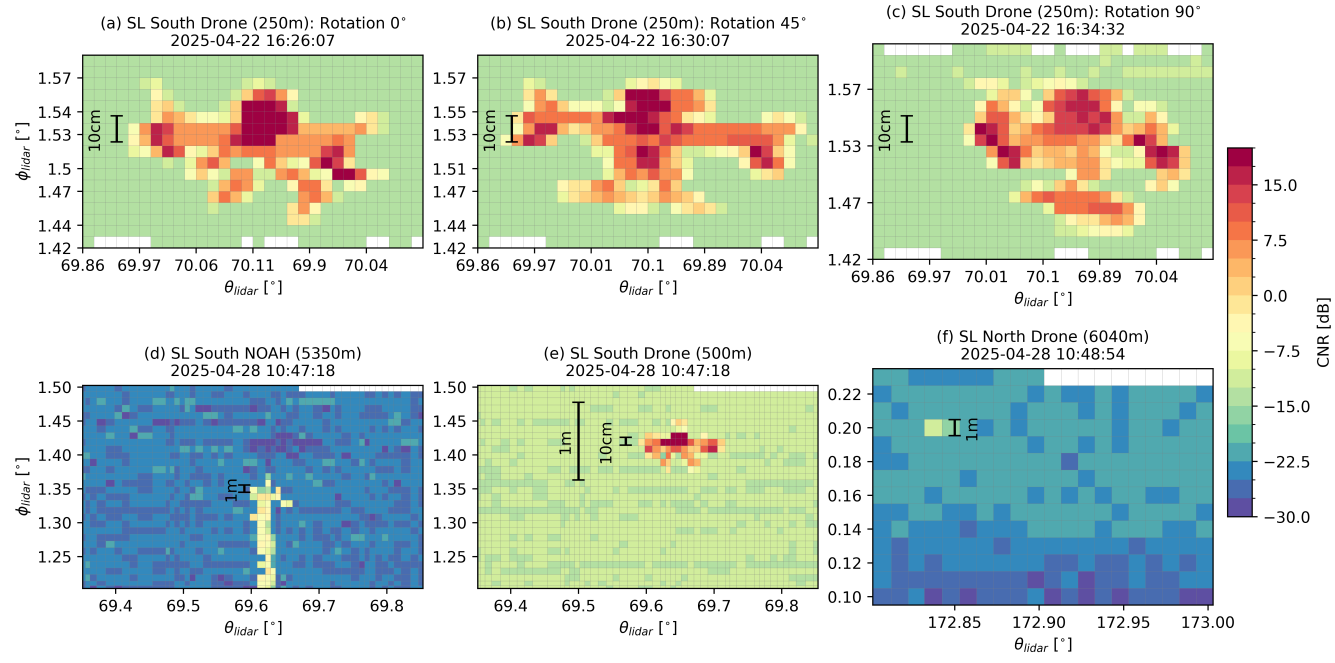

Figure 7. Hard target mapping showing CNR as a function of θ_{lidar} and ϕ_{lidar} across the different flights of drone. Panels (a)-(c) is of flight #1 during rotation test. Panel (d) NOAH and (e) drone acquisition from SL South and (f) drone acquisition from SL North during flight #7 at location D1 and height H1. The angular resolution of the scans are 0.01° in θ and ϕ corresponding to an equivalent horizontal and vertical distances of approximately 0.04 m in (a)-(c), 0.9 m in (d), 0.09 m in (e) and 1.05m (f).

backscatter signature encompasses a single $0.01°$ pixel, removing ambiguity in determining the exact reference location on the drone that is more apparent at short range.

An example of the inter-flight height variation during Flight #7 of multiple drone acquisitions by SL South is illustrated in Figure 8. This flight had the largest number of independent acquisitions of the drone by the lidar at a single height, and experienced the strongest and largest variation in wind speeds ranging from 5.8 m s^{-1} to 13.1 m s^{-1} with a mean of 9.3 m s^{-1} (Table 4). Throughout the flight duration of approximately 25 minutes, the height of the drone as estimated by the RTK positioning system (Fig. 8c) exhibited variations no larger than 0.34 m which is within the vertical extent of the drone of 0.43 m.

The results of ϕ_{off} obtained from the DHT method are presented alongside the SHT results in Figure 9 with mean offset and uncertainties given in Table 8. For SL South, the drone offset at D1 very closely agrees with the reference (NOAH) offset with a difference between the mean offset and reference of $-0.002°$ (Table 8). The mean offset from D1 combined with D2 and D3 flight locations captures the peak of the sinusoid that was estimated from the SHT method (Fig. 9). For SL North, the drone offset is close to the offset estimated in the NOAH direction and the adjacent static hard target and when evaluated alongside the SHT results, indicates little variation in the elevation offset as a function of azimuth compared to SL South. Applying the

https://doi.org/10.5194/wes-2026-94
Preprint. Discussion started: 11 June 2026

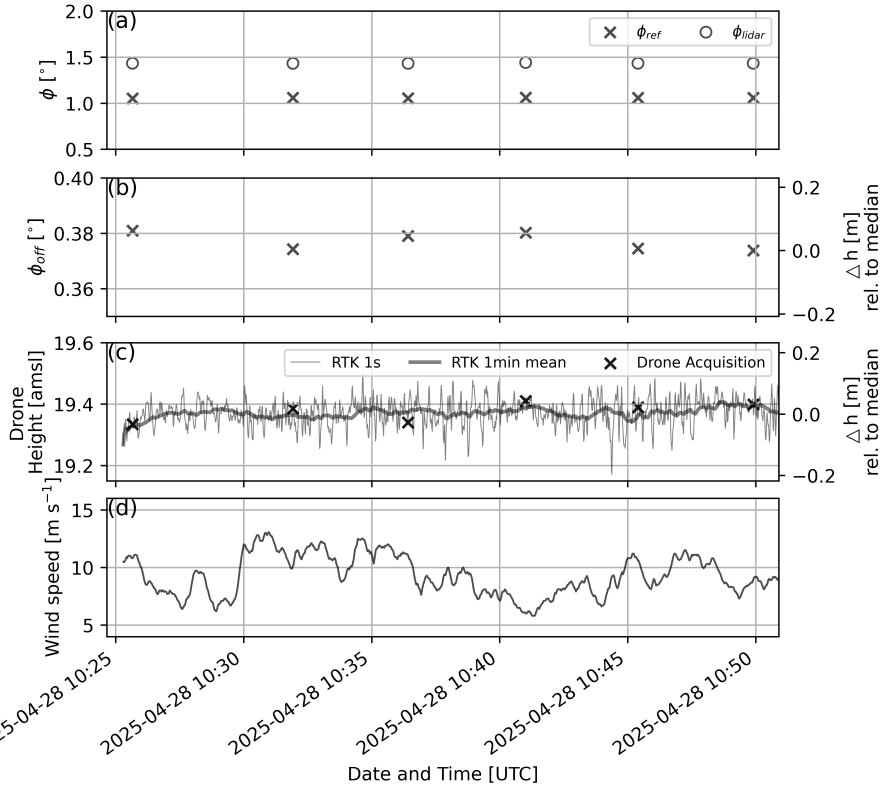

Figure 8. Timeseries of (a) ϕ (ϕ_{ref} and ϕ_{lidar} SL South), (b) ϕ_{off} SL South, (c) drone height determined by RTK position, and (d) ambient wind speed measured by drone during continuous flight #7 at location D1 and height H1. In (b) and (c) the secondary (right hand) y-axis is the height difference, $\triangle h$ [m] of each data point relative to the median height during the flight.

Monte Carlo approach to combined static and drone data for SL North leads to a difference in the predicted elevation offset with respect to the HTT reference of $-0.07°$. This is a 65 % reduction in the difference of the estimated offset in the reference direction relative to applying Monte Carlo extrapolation using only the available SHT candidates (Fig. 6, Section 3.2). Based on the agreement between the drone offsets and the SHT reference offset at SL South, it is expected that if the drone had been flown in the reference SHT direction from SL North, the derived offset from the drone in this direction would be equivalent to the reference. The overall uncertainties of the offsets derived from the DHT method are $\pm 0.03°$, dominated by the systematic uncertainty of $0.03°$.

3.3 Sea Surface Levelling

To examine the overall performance and sensitivity of the SSL method, the SSL results obtained from the RHI and PPI scans at the azimuth of the reference static hard target are shown in Figure 10. The results are shown as a function of lidar elevation angle and summarise median goodness-of-fit parameters R^2 and $\sigma_{r_{\text{ss}}}$ used to filter r_{ss} (Fig. 10a-d), data populations after filtering for

https://doi.org/10.5194/wes-2026-94
Preprint. Discussion started: 11 June 2026

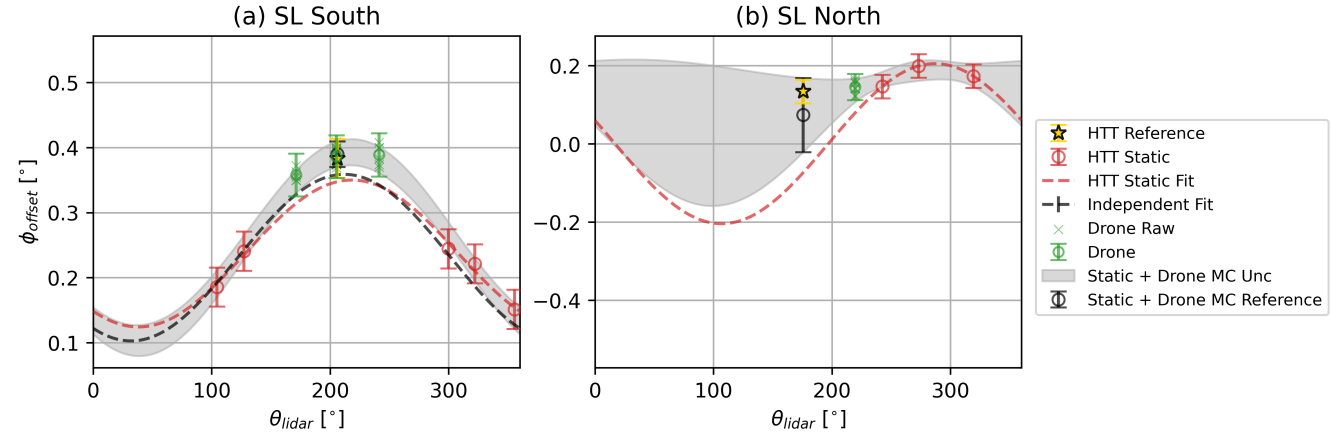

Figure 9. As Figure 6 but with ϕ_{off} determined from drone flights.

Table 8. Summary of ϕ_{off} determined from drone-based hard target scans for SL South and SL North. The static hard target reference for NOAH is also included for comparison.

Lidar	Location	N flights	N	Mean ϕ_{off} [°]	$\sigma_{\phi_{\text{off}}}$ [°]	$u_{\phi_{\text{off}}}$ [°]
SL South	Ref (NOAH)		16	0.384	0.134	0.030
	D1	4	15	0.386	0.012	0.030
	D2	2	6	0.358	0.008	0.030
	D3	2	6	0.389	0.015	0.031
SL North	D1	2	8	0.146	0.017	0.031

goodness-of-fit (Fig. 10e-f), the resulting mean r_{ss} (Fig. 10g-h), and mean ϕ_{off} (Fig. 10g-h) obtained from the method across the same 1.5 day scanning period. Sea conditions were relatively calm with wave heights < 0.7 m during the test.

Overall, the distributions of the goodness-of-fit parameters R^2 and $\sigma_{r_{\text{ss}}}$ indicate that the sigmoid curve fitting method applied to determine r_{ss} is sensitive to elevation angle and thus the angle and distance that the laser beam enters the water. The median R^2 increases with elevation angle, indicating that it is more difficult to obtain accurate curve fits at steeper (more negative) elevation angles and shorter sea surface ranges (< 500 m). In contrast, $\sigma_{r_{\text{ss}}}$, used to indicate the uncertainty in r_{ss} of the fit, markedly increases above 20 m at small positive elevation angles when the beam is near- or above horizontal and it is thus not possible to identify a marked inflection point in the CNR return due to the absence of any beam-sea intersection. Based on these results, relatively conservative goodness-of-fit thresholds of $R^2 > 0.8$ and $\sigma_{r_{\text{ss}}} < 20$ m are applied to remove bad data associated with larger negative and positive elevation angles, leaving approximately 30–50 % of scan data for SL South and 50–90 % of data for SL North. While the distribution of R^2 and $\sigma_{r_{\text{ss}}}$ versus elevation is similar for both lidar units and scan

https://doi.org/10.5194/wes-2026-94
Preprint. Discussion started: 11 June 2026

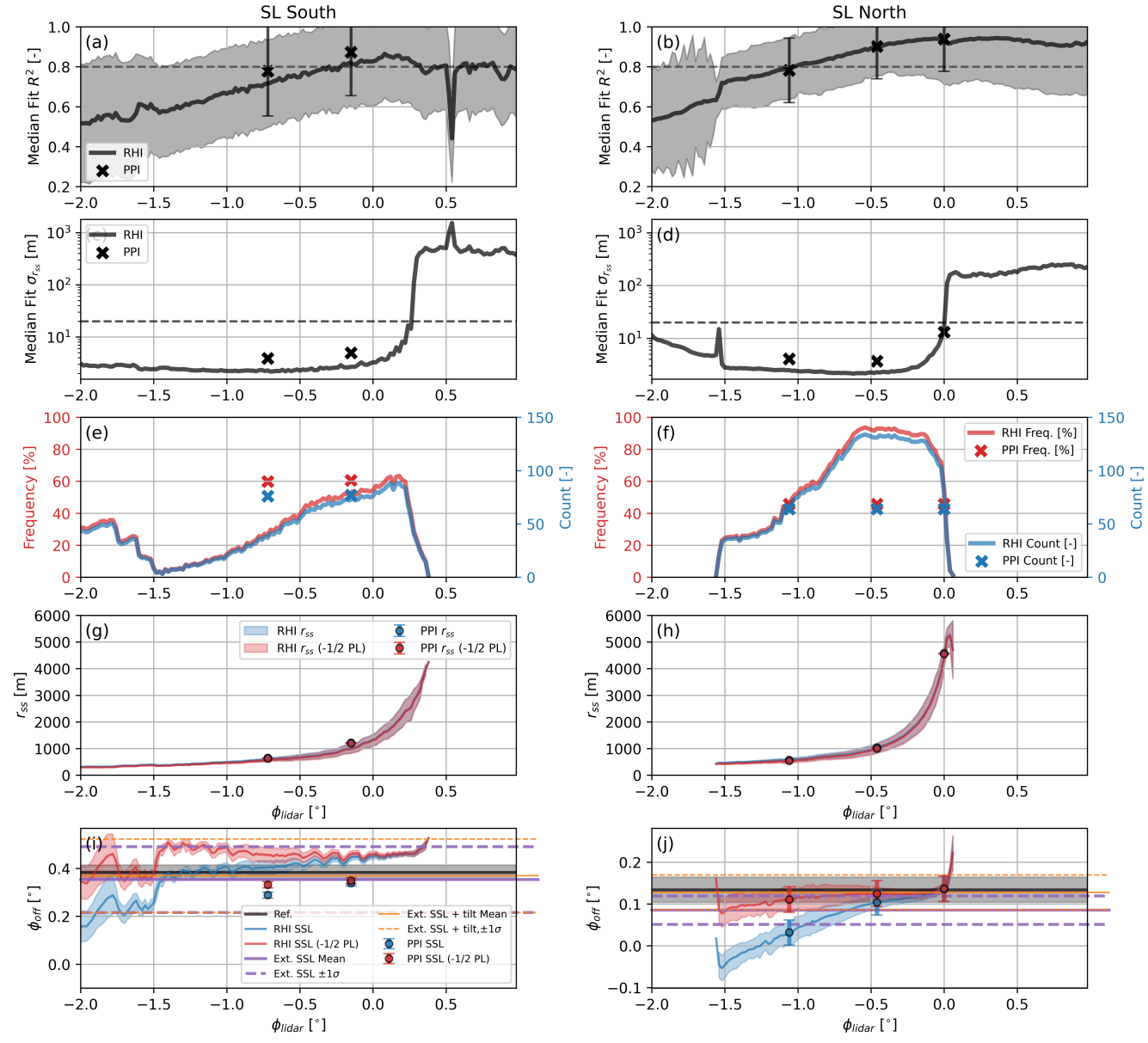

Figure 10. Sea surface levelling results for SL South (left column) and SL North (right column) as a function of lidar scan elevation angle (ϕ_{lidar}) obtained from RHI (lines) and PPI (markers) scan data along the pointing azimuth to the single target reference (NOAH) during common time period of 2025-04-29 00:00UTC to 2025-04-30 12:30UTC. (a)-(b) show the median (line/marker) $\pm 1\sigma$ (shading/error bar) of the r-squared of the sigmoid curve fits used to determine r_{ss}. (c)-(d) show the median $\sigma_{r_{\text{ss}}}$ of the fits with dashed line delineating $\sigma_{r_{\text{ss}}} = 20$ m. (e)-(f) are the resulting data populations after filtering for r-squared > 0.8 and $\sigma_{r_{\text{ss}}} < 20$ m expressed as counts and their frequency relative to the total count. (g)-(h) present the median (line/marker) $\pm 1\sigma$ (shading/error bar) of the sea surface range r_{ss}. (i)-(j) present the mean $\pm 1\sigma$ of ϕ_{off} determined by equations 7 and 8 (mean: solid line, $\pm 1\sigma$ dashed lines). In (g)-(h), the blue line depicts r_{ss} determined from Eq. (9), whereas the red line depicts r_{ss} determined from Eq. (9) corrected by $r_{\text{ss}} - 1/2$ probe length (PL). Similarly, in (i)-(j), the blue line depicts ϕ_{off} determined from Eq. (7) using r_{ss}, whereas red lines depict ϕ_{off} determined from Eq. (7) using $r_{\text{ss}} - 1/2$ PL.

https://doi.org/10.5194/wes-2026-94
Preprint. Discussion started: 11 June 2026

eawe european academy of wind energy
Open Access WIND ENERGY SCIENCE DISCUSSIONS

types at equivalent scan elevation angles, R^2 is higher for scans from SL North compared to SL South which is why a larger proportion of scan data is available for SL North after filtering (Fig. 10e-f).

The resulting elevation offsets also show sensitivity to the lidar elevation angle depending on the methodology applied to obtain ϕ_{off}, the applied scan type (PPI/RHI), and specific device. ϕ_{off} calculated using r_{ss} tends to underestimate the reference (NOAH) offset at increasingly negative elevation angles. This behavior is non-linear for SL South and occurs only across the small elevation angle range of $-2°$ to $-1.5°$, whereas it is strongly linear for SL North where the magnitude of ϕ_{off} underestimation reduces as the elevation angle increases toward zero. Furthermore, a large systematic difference is observed between ϕ_{off} determined from RHI versus PPI scans for SL South whereas the RHI and PPI results agree well for SL North. A direct comparison of the results obtained from the two scan types at equivalent elevation angles is shown in Figure 11. r_{ss} determined from PPI scans are systematically larger than RHI scans at longer ranges for SL South resulting in a lower estimated ϕ_{off} from the PPI data with a mean difference of approximately $0.1°$. In contrast, the mean differences between ϕ_{off} from PPI and RHI scans are $0°$ for SL North. These results suggest that the elevation offsets obtained by the SSL method can vary with scan type depending on the specific device, due to the type of scan head mechanism (e.g. belt driven for SL South and gear driven for SL North), and firmware/software versions depicting scanner head control (1).

Using r_{ss} by corrected by half the probe length ($r_{ss} - 1/2\text{PL}$) leads to an overall flattening of ϕ_{off} as a function of elevation angle, suggesting that the probe length correction successfully accounts for some ambiguity in identifying the sea surface range from the immersion of the laser beam in the water. For both lidars, the correction removes most of the systematic underestimation of the reference elevation offset at more negative (steeper) elevation angles where the sea surface is closer to the lidar and the probe length correction will have a proportionally larger effect on the sea surface range and resulting ϕ_{off}. The correction leads to an overestimation of the reference ϕ_{off} at elevation angles above $-1.5°$ in SL South, whereas the reference ϕ_{off} is underestimated by SL South.

The extended SSL method is applied using the filtered r_{ss} corrected by half the probe length to the RHI scan data across all valid lidar elevation angles per 15-min. Therefore the estimated offset does not vary as a function of elevation angle. The method is applied both including the prediction of α and β (Ext. SSL) and without the prediction of of α and β where the device tilt is given by the pitch and roll measurements from each device inclinometer (Ext. SSL + tilt). For SL South the resulting estimated mean elevation offsets are very similar to the reference for both the Ext. SSL and Ext. SSL + tilt corrected methods. For both methods, the range $\phi_{\text{off}} \pm 1\sigma$ is similar to the variation if ϕ_{off} observed as a function of ϕ_{lidar} for the SSL method. In contrast, for SL North, the standard Ext. SSL method underestimates the reference. However after incorporating for the device tilt, the Ext SSL + tilt method is very similar to the reference. This indicates that the Ext. SSL approach is sensitive to the parameter choice and reducing the number of predicted variables for the curve fit could reduce the uncertainty of the method.

A comparison of the SSL results as a function of lidar azimuth is presented in Figure 12 with a summary of the estimated elevation offsets in Table 9. Overall the estimated elevation offsets from both the SSL RHI, SSL PPI and Extended SSL (RHI) methods are in close agreement with the reference HTT offset for SL North. For SL South, the offsets estimated by the SSL RHI and PPI scans fall above and below the reference, whereas the offsets estimated by the Extended SSL method (RHI) closely agree with the reference HTT offset. The standard uncertainty ($\sigma^2_{\phi_{\text{off}}}/N$) of all the methods is less than $0.01°$ except

https://doi.org/10.5194/wes-2026-94
Preprint. Discussion started: 11 June 2026

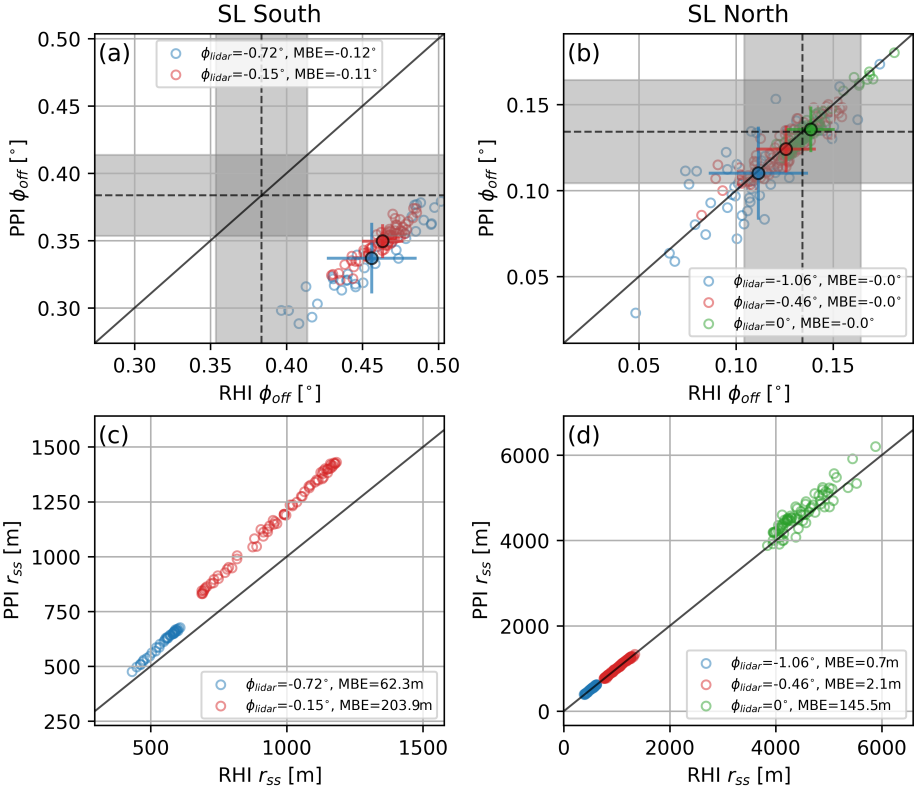

Figure 11. Comparison of SSL results from RHI (x-axis) and PPI (y-axis) scans by SL South (left column) and SL North (right column) obtained at equivalent scan elevation angles (ϕ_{lidar}) per 15-min aggregated scan data along the pointing azimuth to the single static target reference (NOAH). (a)-(b) compares ϕ_{off} for different ϕ_{lidar} where open circles represent the 15-min data, filled circles and error bars represent mean $\phi_{\text{off}} \pm 1\sigma$, and black dashed lines and grey shading delineate the reference static hard target offset $\pm u_{\phi_{\text{off}}}$. Panels (c)-(d) compare 15-min r_{ss}. In both cases ϕ_{off} and r_{ss} depict results corrected by $-1/2$ PL. The 1:1 relationship is denoted by the solid black line and the mean bias error (MBE; mean of the differences: PPI−RHI) for each ϕ_{lidar} is shown in the legend.

https://doi.org/10.5194/wes-2026-94
Preprint. Discussion started: 11 June 2026

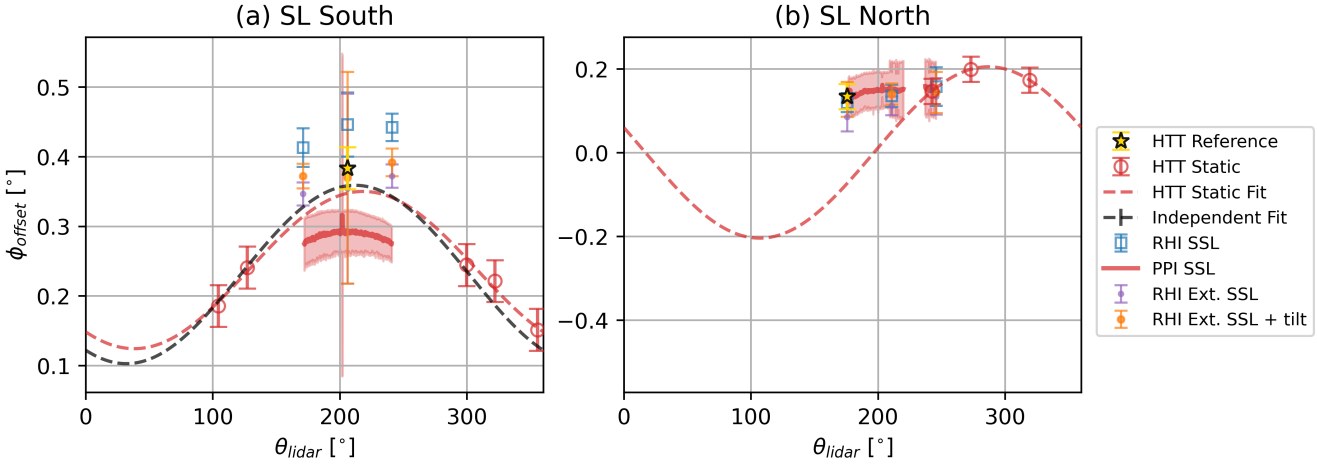

Figure 12. As Figure 6 but with ϕ_{off} determined from sea surface levelling methods. The mean $\phi_{\text{off}} \pm \sigma_{\phi_{\text{off}}}$ across all available elevation angles is shown for the SSL and Extended SSL results.

for the Extended SSL method applied to SL South which is $0.014°$. Overall, the low standard uncertainties show that the SSL methodologies are robust with high repeatability. For SSL only, the mean analytical uncertainty estimates $u_{\phi_{\text{off}}}$ are much larger than the standard uncertainties, with mean values of $0.05°$ to $0.07°$ and maximum values of $0.09°$ to $0.20°$. The larger analytical uncertainty estimates are driven by the tidal height, with maximum uncertainties observed when the tidal height is below mean sea level. Analytical uncertainty values for the Extended SSL method obtained from the covariance matrix of the curve fit were very large and non-physical so are not shown. In contrast, the analytical uncertainties obtained from the Extended SSL + tilt method, which removes the estimation of α and β by the curve fit, yielded mean values of approximately $0.01°$ and $0.1°$, and maximum values of $0.2°$ and $3.1°$ for SL North and SL South, respectively. Both the non-physical output for the Extended SSL method and large variations between the analytical uncertainties derived from the curve fit highlights that both implementations of the Extended SSL method are highly sensitive to the curve fitting process, which is dependent on the number of estimated variables and how well the input r_{ss} and ϕ_{off} can be described by the model.

3.4 Intercomparison

To compare the performance across the three HTT methods, Figure 13 shows timeseries of ϕ_{off} estimated from each method along the azimuthal direction of the reference hard target, and the effective height H_{eff} and pitch and roll estimated by the Ext. SSL method. Some initial scan data for the SSL method was available 1 day prior to the main SSL test period (29 April 2025 to 30 April 2025) and has been included for reference. Only DHT results from drone flights on the 28 April 2025 (flights #7 and #8) are shown as these are closest in time to the SSL test period. As indicated previously in Sections 3.2 and 3.3, the DHT method is very close to the reference offset whereas the SSL methods show varying performance depending on the specific lidar and method applied. Temporal variations in ϕ_{off} are observed in the SSL results which are attributable to device tilt and/or

https://doi.org/10.5194/wes-2026-94
Preprint. Discussion started: 11 June 2026

eawe european academy of wind energy
Open Access WIND ENERGY SCIENCE DISCUSSIONS

Table 9. Sea surface levelling results from scan data in the azimuthal direction of the reference hard target (NOAH).

Method		SSL RHI	SSL PPI	SSL Ext.	SSL Ext. + tilt
SL South	N*	5164	87	115	116
	ϕ_{off} Mean [°]	0.446	0.325	0.354	0.370
	ϕ_{off} Median [°]	0.456	0.333	0.390	0.411
	$\sigma_{\phi_{\text{off}}}$ [°]	0.046	0.027	0.136	0.152
	$\sigma^2_{\phi_{\text{off}}}/N$ [°]	0.001	0.003	0.013	0.014
	$u_{\phi_{\text{off}}}$ analytical (mean) [°]	0.071	0.047	–	0.085
	$u_{\phi_{\text{off}}}$ analytical (max) [°]	0.199	0.088	–	3.125
SL North	N*	7082	179	138	138
	ϕ_{off} Mean [°]	0.120	0.127	0.085	0.128
	ϕ_{off} Median [°]	0.122	0.128	0.087	0.130
	$\sigma_{\phi_{\text{off}}}$ [°]	0.023	0.021	0.034	0.041
	$\sigma^2_{\phi_{\text{off}}}/N$ [°]	0.000	0.002	0.003	0.004
	$u_{\phi_{\text{off}}}$ analytical (mean) [°]	0.047	0.043	–	0.005
	$u_{\phi_{\text{off}}}$ analytical (max) [°]	0.125	0.098	–	0.184

*Note, N samples are substantially higher for SSL RHI because the statistics are of ϕ_{off} for multiple ϕ_{lidar} (up to 150) times the number of 15-min timestamps during the scanning period. In contrast, SSL PPI and SSL Ext yield a single estimate of ϕ_{off} every 15-min and therefore have a lower and similar sample size.

sea state conditions during the test. For example, SL South experienced an increase in pitch/roll during 29 April 2025 which appears correlated with the variation in elevation offset estimated by the SSL RHI and SSL PPI scans during the same period. The pitch and roll estimated by Ext. SSL method have a similar distribution to the lidar inclinometer values for SL South although they are higher and lower, respectively, than the device inclinometer readings. In contrast the estimated pitch and roll values are the same for SL North and disagree with the device inclinometer readings. While wave conditions in the vicinity of the test area were very calm with very small wave height variations < 1 m throughout the whole test, during the 12 hour period from 2025-04-29 18:00 until 2025-04-30 06:00, wave heights became more variable which may have contributed to some of the variability in ϕ_{off} estimated from the SSL methods throughout this time. However, using wave simulation Gramitzky et al. (2026) have shown that the impact of significant wave heights of 1 m on ϕ_{off} is expected to be less than $0.04°$ across a range of small and large wavelengths. The effective height H_{eff} estimates from the Ext. SSL method are in close agreement with the reference estimate using the tide gauge measurements from North Shields although differences can be attributed to the different location of the tide gauge and remaining noise in the scan data.

Figure 14 compares the estimated elevation offsets from all methods as a function of lidar azimuth. Across all methods the results generally capture the similar magnitude of the reference ϕ_{off} with some variations that can be attributed to the different methodologies. The SHT method is most limited by the onsite hard targets available to each device, with the sine curve

https://doi.org/10.5194/wes-2026-94
Preprint. Discussion started: 11 June 2026

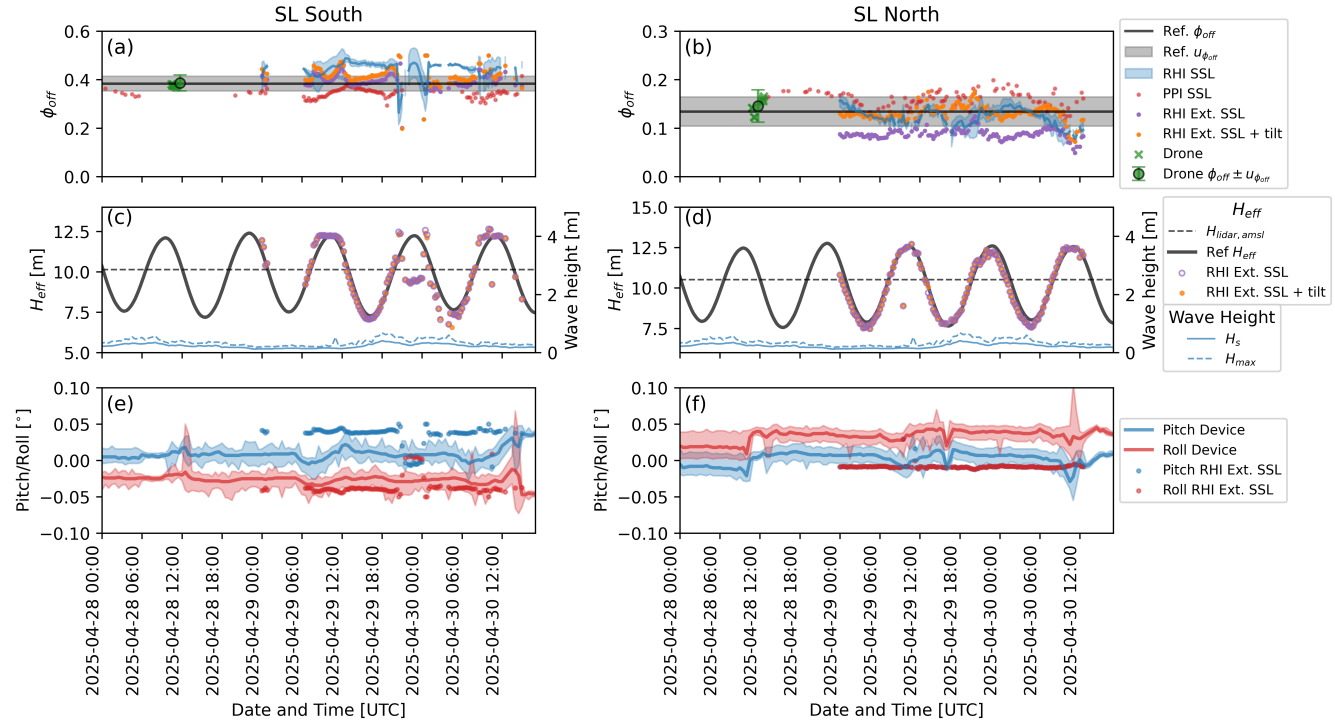

Figure 13. Timeseries for SL South (left) and SL North (right) showing (a,b) elevation offsets determined at the NOAH reference Azimuth from each method, (c,d) effective heights H_{eff} estimated by each SSL method, and wave heights measured by nearby Waverider buoy, and (e,f) lidar pitch and roll.

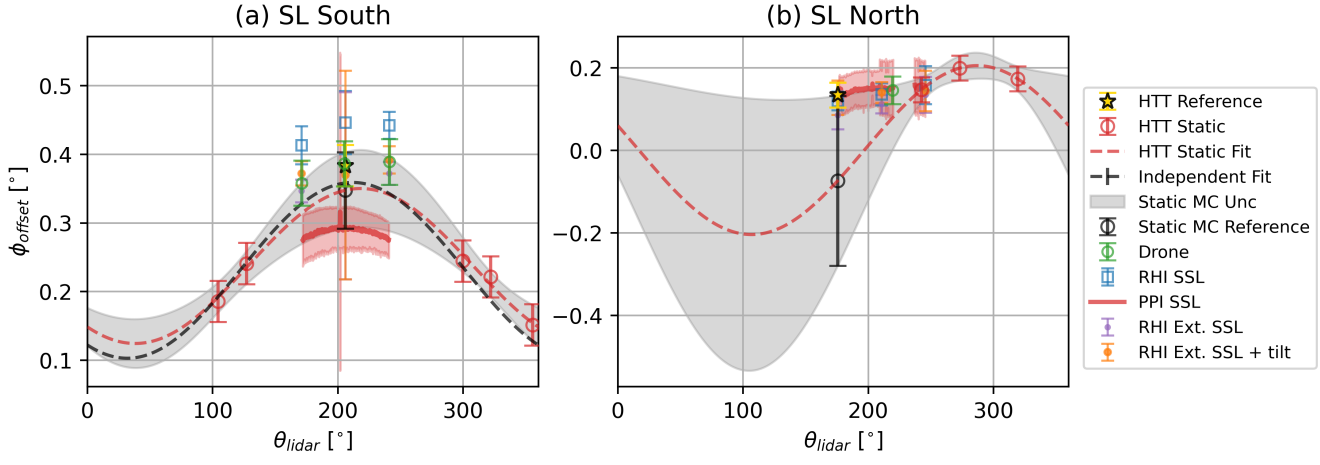

Figure 14. As Figure 6 with ϕ_{off} determined from all HTT methods.

https://doi.org/10.5194/wes-2026-94
Preprint. Discussion started: 11 June 2026

eawe european academy of wind energy
Open Access WIND ENERGY SCIENCE DISCUSSIONS

Table 10. Overall results in desired campaign pointing direction (NOAH) from HTT methods. For SSL method the results are aggregated across all scan elevation angles. For SL North, drone measurements never taken in mast direction so not included in comparison.

HT Method	UQ method	$\phi_{\text{off}} \pm u_{\phi_{\text{off}}}$ [°]		Difference ϕ_{off} with Reference [°]	
		SL South	SL North	SL South	SL North
SHT Reference (NOAH)	Analytical	0.38 ± 0.03	0.13 ± 0.03	–	–
SHT	Monte Carlo	0.35 ± 0.06	-0.07 ± 0.21	-0.03	-0.20
DHT	Analytical	0.38 ± 0.03	± 0.03	0.004	–
SHT + DHT	Monte Carlo	0.39 ± 0.02	0.07 ± 0.10	0.01	-0.06
SSL RHI	Analytical (mean u_{off}/max u_{off})	$0.45 \pm 0.07/0.20$	$0.12 \pm 0.05/0.12$	0.07	-0.01
SSL PPI	Analytical (mean u_{off}/max u_{off})	$0.33 \pm 0.05/0.09$	$0.13 \pm 0.04/0.10$	-0.05	0.00
SSL Ext.	Analytical (mean u_{off}/max u_{off})	$0.35 \pm -$	$0.09 \pm -$	-0.03	-0.04
SSL Ext. + tilt	Analytical (mean u_{off}/max u_{off})	$0.37 \pm 0.09/3.13$	$0.13 \pm 0.01/0.18$	-0.01	0.00

extrapolation more successful for SL South due to the larger number of hard targets and their wider azimuthal distribution. Overall, methods pointing exactly in the azimuthal direction of the reference agree closest to the reference; namely the DHT method and both Extended SSL methods (Table 9). The differences between the mean elevation offset derived from each method and the reference target range from $-0.03°$ to $-0.20°$ for SHT, $-0.002°$ for DHT, and from $-0.05°$ to $+0.07°$ across all SSL and SSL extended methods. The SSL method performs similarly well for both RHI and PPI scan strategies applied to SL North, however the results for the same scan configurations applied to SL South are less consistent with RHI scans overestimating the reference and PPI scans underestimating the reference. The overall uncertainties are approximately $\pm 0.03°$ for the SHT and DHT methods, dominated by $u_{\phi_{\text{lidar,sys}}} = 0.03°$. The uncertainties are largest for the SSL method with magnitudes of up $\pm 0.1°$ to $\pm 0.2°$, driven by tidal variations.

4 Discussion

The results presented in this paper show that the static elevation offset of scanning lidar can be determined to varying levels of accuracy using different HTT methodologies. The findings therefore have implications on the suitability of the different methodologies in determining the elevation offset and height positioning uncertainty for a wind measurement campaign. Differences between the mean elevation offset derived from each method and the reference hard target range from $-0.03°$ to $-0.20°$ for SHT, $-0.002°$ for DHT, and from $-0.05°$ to $+0.07°$ for SSL. The uncertainties found from the methods range from approximately $0.03°$ (DHT) to up to $0.20°$ (SHT extrapolated/SSL). An example of the implications of these differences and uncertainties on beam height and thus wind speed errors for measurements obtained at different ranges and vertical wind shears is shown in Figure 15. In Figure 15 the horizontal wind speed errors are calculated based on using the wind profile power

https://doi.org/10.5194/wes-2026-94
Preprint. Discussion started: 11 June 2026

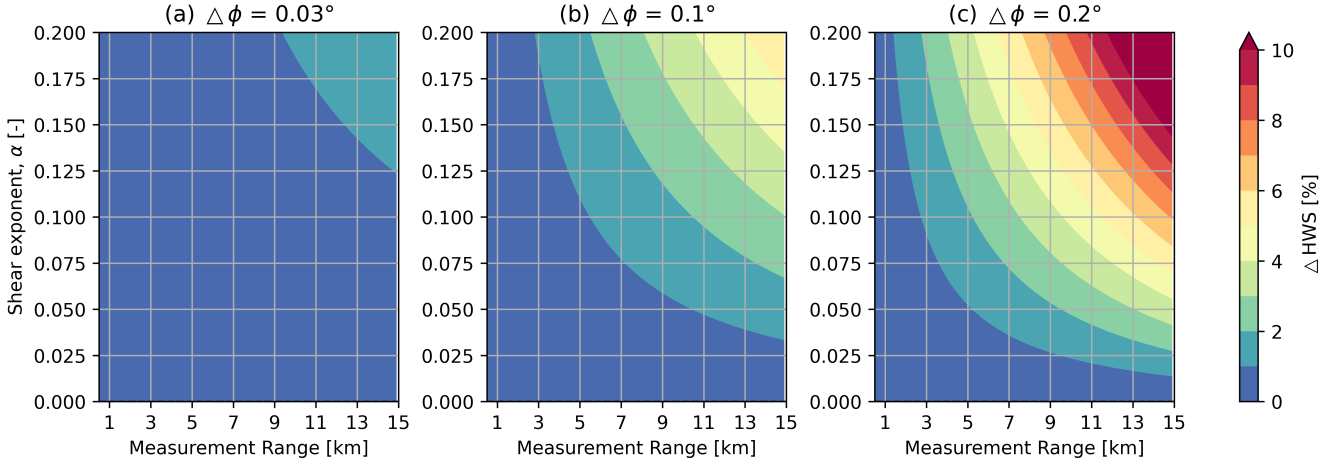

Figure 15. Percentage change in a horizontal wind speed ($\triangle HWS$) of 10 m s^{-1} vertically extrapolated from 100 m downwards by the equivalent height deviation expected due to $\triangle\phi$ at different measurement ranges and shear coefficients.

law to vertically extrapolate a wind speed of 10 m s^{-1} at 100 m using a range of shear exponents (α) down to a new height equal to 100 m minus the equivalent height variation due to an elevation angle deviation of $\triangle\phi$ across different measurement ranges. For example, using the elevation offset and uncertainty determined from the DHT method, elevation errors of $0.03°$ correspond to height differences of up to 6 m at 15 km. This height variation would result in a wind speed error of 1.2 % in high shear ($\alpha = 0.15$) conditions and an error of 0.6 % in relatively low shear conditions ($\alpha = 0.07$) representative of offshore conditions. Conversely, errors of $0.1°$ (for example seen for the SSL method) would lead to equivalent height errors of 9 m at 5 km, 18 m at 10 km and 26 m at 15 km. Such height errors correspond to wind speed errors of 1.4 %, 2.8 % and 4.5 % in high shear, and 0.6 %, 1.3 % and 2.1 % in low shear conditions, respectively, with the uncertainties approximately doubling these values for the worst case error of $0.2°$ found across the hard targeting methods. As wind lidar technology develops to provide measurements at longer ranges, minimising beam height positioning errors will become more important.

In practical terms, the suitability of the different methods is likely to depend on the context of a given lidar deployment and its application. In the context of this experiment, for near-shore deployments with no-offshore hard target, the DHT method has been shown to be the most flexible approach with smallest uncertainty. The drone can be flown to multiple azimuths and used to determine the azimuthal variation of the elevation offset to high accuracy. However, the disadvantage of the DHT method is that it is the most logistically complex and expensive to execute. The method is time intensive (setup and test execution), limited by site dependent flight restrictions, weather, drone flight duration, and requires more personnel (drone and lidar operators) to carry out. While the SHT method is the simplest approach, the method is sensitive to the number and azimuthal spread of available targets which is a limiting factor for near-shore deployments. An alternative approach, that was not examined here, is to use a single hard target and repeat hard target scans of the target for different physical rotations of the lidar body (e.g. every $90°$) to obtain the elevation offset as a function of azimuth (NEDO, 2023). However, this method is also time intensive

https://doi.org/10.5194/wes-2026-94
Preprint. Discussion started: 11 June 2026

and requires the device to be leveled to the same precision each time. In theory, the sea surface levelling methods are the least practically restrictive; sea surface scans can be programmed initially to determine the elevation offset and its variation with azimuth, then scheduled regularly in between measurements to track the pointing stability throughout a measurement campaign. If tidal measurements are unavailable, the extended SSL method shows capability in estimating tidal height variations (Fig. 13) and furthermore the SSL method could also be combined with a tidal model to account for tidal height particularly for near-shore deployments with a large tidal range. However, as shown in the results presented here, the SSL method exhibits larger uncertainties, sensitivity to the determination of the exact sea surface range, and exhibits differences across two different lidars with different scan head designs. The SSL method relies heavily on data post-processing and curve fitting procedures and therefore is highly sensitive to how well the input data populations can be described by the respective model(s). Another consideration is how frequently do SSL measurements need to be made to obtain an unbiased measurement of the elevation offset considering sea state and device tilt. Such factors should be investigated in future work.

While this study has compared different hard targeting methodologies in a consistent and systematic manner, there are some further limitations of the experiment which are important to acknowledge. The two scanning lidars tested were deployed at different locations and therefore it was not possible to use the same SHT candidates for both devices and also perform DHT method consistently across both systems, which would have been possible if both devices were located side-by-side. Another limitation is that the lidar devices tested are two versions of the same type from the same manufacturer. Therefore it is unknown how transferrable the findings are to other types of scanning lidar devices. The experiment is also representative of a static-surface coastal deployment situation. Therefore the implications are different for offshore deployments installed on wind turbine transition pieces or nacelles where the devices are subject to more movement and where the remote situation of the deployment poses more logistical challenges. In such situations, SSL methods are clearly the most logistically suitable to employ, but based on the results of this study, it is recommended that where possible these methods are verified using SHT (e.g. nearby turbine) or DHT (drone) methods to help reduce their uncertainty. Finally, the clear differences between HTT methods evaluated, and their resulting uncertainties are recommended to be considered during the standardisation of scanning lidar for wind energy applications which is currently in development.

5 Conclusions

This paper has systematically evaluated and compared the performance of three HTT methodologies in determining the elevation angle offset for scanning lidar wind measurement campaigns with the aim of quantifying and understanding their accuracy and uncertainty. The comparison was conducted using two independent Vaisala WindCube WLS400S scanning lidar devices (SL South and SL North), at a near-shore (coastal) wind measurement test site in the UK. The three applied methodologies were static hard targeting, dynamic hard targeting using a drone, and sea surface levelling with uncertainties quantified for each method. The methods were deployed coherently across the two devices for their inter-comparison and verification against a reference elevation offset obtained from an offshore reference hard target (meteorological mast).

https://doi.org/10.5194/wes-2026-94
Preprint. Discussion started: 11 June 2026

eawe european academy of wind energy
Open Access WIND ENERGY SCIENCE DISCUSSIONS

Unsurprisingly, the SHT method was sensitive to the number and spread of suitable onshore hard target candidates available to each lidar with unobstructed field of view which is the main constraint of this method. The method performed best for SL South which had 5 targets distributed across a wide azimuthal range of $251°$, leading to only a difference of $-0.03°$ in the predicted offset from the method relative to the reference hard target. In contrast, a large difference of $-0.2°$ in the predicted offset from the method relative to the reference hard target was obtained for SL North using only 3 targets distributed over a narrow azimuthal range of $77°$. These differences corresponded to beam height positioning errors of approximately 3 m and 24 m at the reference target range of 5.3 km and 6.8 km for SL South and SL North, respectively.

The DHT method with the drone provided more flexibility than the SHT method as the hard target (drone) could be flown in the desired pointing direction of the lidar, which in this case was the reference target direction. A difference of $0.002°$ was found between the mean elevation offset obtained from 15 acquisitions of the drone over 4 flights at close range (500 m) by SL South with respect to the reference, corresponding to a height difference of approximately 0.2 m at the reference range of 5.3 km. 8 acquisitions of the drone over 2 flights were also made at long range (6 km) by SL North illustrating the additional flexibility of the method at both near and far ranges. The drone remained stable to within 2 m horizontally and 0.4 m vertically across all flights over a range of mean wind speeds from 2 to 9 m s^{-1} with a maximum of 13 m s^{-1}.

The SSL method was employed using both RHI and PPI scans aligned with the azimuths of the drone flights and reference target. The RHI and PPI scan data were programmed to intersect the sea-surface at different elevation and azimuth angles and the CNR variation with range from the lidar was used to determine the distance of the sea surface using a sigmoid function. Two SSL methods were tested - the first (SSL RHI/PPI) estimated the elevation offset at each lidar azimuth and elevation angle from the sea surface range, whereas the second (Extended SSL) estimated the elevation offset across all elevation angles by applying a curve fit to the lidar elevation angle and sea surface range. Overall the elevation offsets obtained from the SSL RHI/PPI method exhibited variations with the lidar scan elevation angle, suggesting sensitivity of the method to the range of the sea surface, associated with uncertainty in distinguishing the sea surface due to the partial immersion of the probe volume by the water. Applying a recommended correction of 1/2 probe length to the sea surface range (Gramitzky et al., 2026) led to a reduction in this uncertainty, reducing some of the elevation offset dependence with scan elevation angle and thus sea surface range. The mean elevation offset of the extended SSL method applied to the RHI scan data agreed with the reference to within $0.01°$ for both lidar units. However, the estimated elevation offsets determined by the SSL method varied depending on the device. The estimated mean elevation offsets from the SSL method were very consistent between both RHI and PPI sea surface scans for SL North, with agreement with the reference offset of within $0.01°$. However, the results were different for SL South, with estimated mean offsets from RHI scans $0.07°$ larger and PPI scans $0.05°$ smaller than the reference. This difference is considered to be due to the different scanner head mechanisms of the two devices. It also highlights that the SSL method may not be easily extendable to different devices, without proper verification of the SSL method for a specific unit.

Overall the comparison of all methods indicated that the DHT method estimated the elevation offset closest to the reference since it was flown exactly in the azimuthal direction of the reference and is a hard object (like the reference). An uncertainty of $\pm 0.03°$ was obtained for the DHT method and reference. The SHT method was limited in this experiment by the available targets but may provide reliable results if enough targets with sufficient azimuthal spacing were available for a given deployment.

https://doi.org/10.5194/wes-2026-94
Preprint. Discussion started: 11 June 2026

eawe european academy of wind energy
Open Access WIND ENERGY SCIENCE DISCUSSIONS

The uncertainty of the SHT method extrapolated to the reference azimuth by the Monte Carlo approach ranged from $\pm 0.06^\circ$ (SL South) to $\pm 0.21^\circ$ (SL North). While the SSL methods were able to obtain elevation offsets directly in the reference target direction, the results showed much higher variability. The method was sensitive to multiple factors including the ability to accurately determine the sea surface range due to the probe volume, the scan type (RHI/PPI), elevation angle, sea state, and lidar tilt. Despite this, the mean analytical uncertainties estimated for the SSL methods ranged between $\pm 0.01^\circ$ to $\pm 0.1^\circ$ which is inline with the specified angular positioning error ($\pm 0.1^\circ$) of the scanning lidar models.

The implications of these findings suggest that in the absence of static hard target(s) in the desired measurement direction(s) for a campaign, beam positioning errors can be minimised using the DHT method. However, the DHT method is more logistically complex, time intensive and therefore expensive to implement than the other methods which also make it more difficult to employ regularly throughout a campaign to track pointing stability. In contrast, the SSL method can be easily automated prior to and during a campaign, however requires more scrutiny due to the number of factors contributing to its larger uncertainty. Future work should further focus on understanding scanner head mechanism effects on lidar control, improving quantification of the sea surface range, and the use of tidal models in determining the sea surface height at coastal sites.

Author contributions. AO and JG acquired the funding for this research and came up with the initial concept for this study. MY and MD conducted the analysis with support from LH, and wrote the first draft of the manuscript. MY finalised the results and wrote the final draft. MD, LH and MY performed the experiment, including site survey (LH, MY), drone operation (LH) and lidar setup and control (MD). AO and JG supervised the study. All authors contributed to the development of the study and review of the manuscript.

Competing interests. One of the authors is a member of the editorial board of *Wind Energy Science*.

Financial support. Part of this research has been supported by the "NEMO – New methods for turbulence measurements and models in offshore wind" project funded within the Fraunhofer-Gesellschaft ICON programme.

Acknowledgements. We would like to thank both Vaisala and the Oldbaum Services operations teams for their logistical and technical support for the lidar devices used in this study. Tidal data for North Shields from the UK Tide Gauge Network (https://ntslf.org/tides/uk-network) were obtained using Environment Agency tide gauge data from the real-time data API (Beta; https://environment.data.gov.uk/flood-monitoring/doc/tidegauge). Newbiggin Waverider buoy data were obtained from the Northeast Regional Coastal Monitoring Programme https://coastalmonitoring.org/realtimedata/.

https://doi.org/10.5194/wes-2026-94
Preprint. Discussion started: 11 June 2026

eawe european academy of wind energy
Open Access WIND ENERGY SCIENCE DISCUSSIONS

References

Bodini, N., Zardi, D., and Lundquist, J. K.: Three-dimensional structure of wind turbine wakes as measured by scanning lidar, Atmospheric Measurement Techniques, 10, 2881–2896, https://doi.org/10.5194/amt-10-2881-2017, 2017.

Cañadillas, B., Beckenbauer, M., Trujillo, J. J., Dörenkämper, M., Foreman, R., Neumann, T., and Lampert, A.: Offshore wind farm cluster wakes as observed by long-range-scanning wind lidar measurements and mesoscale modeling, Wind Energy Science, 7, 1241–1262, https://doi.org/10.5194/wes-7-1241-2022, 2022.

Champneys, D., Frühmann, R., Menke, R., Sathiyanarayanan, D., and Steger, M.: Guidelines on dual scanning lidar measurements for wind resource assessments, Tech. rep., DNV, Vaisala, 2024.

Ghilani, C. D. and Wolf, P. R.: Elementary Surveying: An Introduction to Geomatics, Prentice Hall, 13 edn., ISBN 978-0-13-255434-3, 2012.

Global Wind Energy Council: Global Wind Energy Council, Tech. rep., https://www.gwec.net/reports/globalwindreport#Download, (last access 22 May 2026), 2026.

Goit, J. P., Yamaguchi, A., and Ishihara, T.: Measurement and Prediction of Wind Fields at an Offshore Site by Scanning Doppler LiDAR and WRF, Atmosphere, 11, https://doi.org/10.3390/atmos11050442, 2020.

Gottschall, J., Gribben, B., Stein, D., and Würth, I.: Floating lidar as an advanced offshore wind speed measurement technique: current technology status and gap analysis in regard to full maturity, WIREs Energy and Environment, 6, e250, https://doi.org/https://doi.org/10.1002/wene.250, 2017.

Gramitzky, K., Jäger, F., Hildebrand, T., Gloria, N., Riechert, J., Steger, M., and Pauscher, L.: Alignment calibration and correction for offshore wind measurements using scanning lidars, Journal of Physics: Conference Series, 2767, 042 014, https://doi.org/10.1088/1742-6596/2767/4/042014, 2024.

Gramitzky, K., Jäger, F., Callies, D., Hildebrand, T., Lundquist, J. K., and Pauscher, L.: Alignment of scanning lidars in offshore campaigns – an extension of the sea surface levelling method, Wind Energy Science, 11, 861–882, https://doi.org/10.5194/wes-11-861-2026, 2026.

Hildebrand, T., Jäger, F., Gloria, N., Michaelis, L., Krasnov, A., Callies, D., Riechert, J., and Pauscher, L.: Offshore wakes measured by an adaptive dual-Doppler scanning lidar system, Journal of Physics: Conference Series, 3025, 012 005, https://doi.org/10.1088/1742-6596/3025/1/012005, 2025.

Hung, L.-Y., Santos, P., and Gottschall, J.: A comprehensive procedure to process scanning lidar data for engineering wake model validation, Journal of Physics: Conference Series, 2265, 022 091, https://doi.org/10.1088/1742-6596/2265/2/022091, 2022.

Krishnamurthy, R., Reuder, J., Svardal, B., Fernando, H., and Jakobsen, J.: Offshore Wind Turbine Wake characteristics using Scanning Doppler Lidar, Energy Procedia, 137, 428–442, https://doi.org/https://doi.org/10.1016/j.egypro.2017.10.367, 14th Deep Sea Offshore Wind RD Conference, EERA DeepWind'2017, 2017.

Menke, R., Vasiljević, N., Wagner, J., Oncley, S. P., and Mann, J.: Multi-lidar wind resource mapping in complex terrain, Wind Energy Science, 5, 1059–1073, https://doi.org/10.5194/wes-5-1059-2020, 2020.

NEDO: Energy and Industrial Technology Development Organization (NEDO) Offshore wind measurement guidebook, New Energy and Industrial Technology Development Organization (NEDO), https://www.nedo.go.jp/content/100962731.pdf, 2023.

Oldroyd, A., Young, M., Docherty, M., Bost, J., Redford, S., Haize, J., Royle, J., and Gottschall, J.: Comparison of classical and drone based hard-target methodologies applied to scanning lidar for offshore wind, in: Journal of Physics: Conference Series, vol. 2875, p. 012041, IOP Publishing, 2024.

https://doi.org/10.5194/wes-2026-94
Preprint. Discussion started: 11 June 2026

Peña, A. and Mann, J.: Turbulence Measurements with Dual-Doppler Scanning Lidars, Remote Sensing, 11, https://doi.org/10.3390/rs11202444, 2019.

Rott, A., Schneemann, J., Theuer, F., Trujillo Quintero, J. J., and Kühn, M.: Alignment of scanning lidars in offshore wind farms, Wind Energy Science, 7, 283–297, https://doi.org/10.5194/wes-7-283-2022, 2022.

Schneemann, J., Rott, A., Dörenkämper, M., Steinfeld, G., and Kühn, M.: Cluster wakes impact on a far-distant offshore wind farm's power, Wind Energy Science, 5, 29–49, https://doi.org/10.5194/wes-5-29-2020, 2020.

Shimada, S., Kogaki, T., Konagaya, M., Mito, T., Araki, R., Ueda, Y., and Ohsawa, T.: Validation of near-shore wind measurements using a dual scanning light detection and ranging system, Wind Energy, 25, 1555–1572, https://doi.org/https://doi.org/10.1002/we.2757, 2022.

Shimada, S., Kogaki, T., Konagaya, M., Mito, T., Misaki, T., Hamada, K., Araki, R., Ohhata, S., Ueda, Y., and Ohsawa, T.: Mutsu 2020 Scanning LiDAR Experiment: Comparison of Dual and Single Scanning LiDAR Systems for Near-Shore Wind Measurement, Wind Energy, 28, e70 003, https://doi.org/https://doi.org/10.1002/we.70003, e70003 we.70003, 2025.

The Crown Estate: UK Offshore Wind Report 2025, Tech. rep., The Crown Estate, https://www.thecrownestate.co.uk/our-business/marine/offshore-wind-report-2025, (last access 22 May 2026), 2025.

Thorsen, G., Simon, E., and Clausen, E.: Drone-based scanning lidar pointing calibration (D4.4), DTU Wind and Energy Systems, 2023.

Trujillo, J.-J., Bingöl, F., Larsen, G. C., Mann, J., and Kühn, M.: Light detection and ranging measurements of wake dynamics. Part II: two-dimensional scanning, Wind Energy, 14, 61–75, https://doi.org/https://doi.org/10.1002/we.402, 2011.

Vasiljević, N., Lea, G., Courtney, M., Cariou, J.-P., Mann, J., and Mikkelsen, T.: Long-Range WindScanner System, Remote Sensing, 8, https://doi.org/10.3390/rs8110896, 2016.

Wang, H. and Barthelmie, R. J.: Wind turbine wake detection with a single Doppler wind lidar, Journal of Physics: Conference Series, 625, 012 017, https://doi.org/10.1088/1742-6596/625/1/012017, 2015.

Wind Europe: Wind energy in Europe, 2025 Statistics and the outlook for 2026-2030, Tech. rep., Wind Europe, https://windeurope.org/data/products/wind-energy-in-europe-2025-statistics-and-the-outlook-for-2026-2030/, (last access 22 May 2026), 2026.